Geophysical Journal International

Geophys. J. Int. (2016) **207,** 1796–1817
Advance Access publication 2016 September 14
GJI Seismology

doi: 10.1093/gji/ggw342

Oceanic lithospheric *S*-wave velocities from the analysis of *P*-wave polarization at the ocean floor

Katrin Hannemann,[1] Frank Krüger,[2] Torsten Dahm[2,3] and Dietrich Lange[1]

[1] *GEOMAR, Helmholtz Centre for Ocean Research Kiel, Kiel, Germany. E-mail: khannemann@geomar.de*
[2] *Institute of Earth and Environmental Science, University of Potsdam, Potsdam-Golm, Germany*
[3] *Section* 2.1, *Physics of Earthquakes and Volcanoes, GFZ Potsdam, Potsdam, Germany*

Accepted 2016 September 14. Received 2016 August 29; in original form 2016 March 22; Editorial Decision 2016 September 12

SUMMARY

Our knowledge of the absolute *S*-wave velocities of the oceanic lithosphere is mainly based on global surface wave tomography, local active seismic or compliance measurements using oceanic infragravity waves. The results of tomography give a rather smooth picture of the actual *S*-wave velocity structure and local measurements have limitations regarding the range of elastic parameters or the geometry of the measurement. Here, we use the *P*-wave polarization (apparent *P*-wave incidence angle) of teleseismic events to investigate the *S*-wave velocity structure of the oceanic crust and the upper tens of kilometres of the mantle beneath single stations. In this study, we present an up to our knowledge new relation of the apparent *P*-wave incidence angle at the ocean bottom dependent on the half-space *S*-wave velocity. We analyse the angle in different period ranges at ocean bottom stations (OBSs) to derive apparent *S*-wave velocity profiles. These profiles are dependent on the *S*-wave velocity as well as on the thickness of the layers in the subsurface. Consequently, their interpretation results in a set of equally valid models. We analyse the apparent *P*-wave incidence angles of an OBS data set which was collected in the Eastern Mid Atlantic. We are able to determine reasonable *S*-wave-velocity-depth models by a three-step quantitative modelling after a manual data quality control, although layer resonance sometimes influences the estimated apparent *S*-wave velocities. The apparent *S*-wave velocity profiles are well explained by an oceanic PREM model in which the upper part is replaced by four layers consisting of a water column, a sediment, a crust and a layer representing the uppermost mantle. The obtained sediment has a thickness between 0.3 and 0.9 km with *S*-wave velocities between 0.7 and 1.4 km s^{-1}. The estimated total crustal thickness varies between 4 and 10 km with *S*-wave velocities between 3.5 and 4.3 km s^{-1}. We find a slight increase of the total crustal thickness from ∼5 to ∼8 km towards the South in the direction of a major plate boundary, the Gloria Fault. The observed crustal thickening can be related with the known dominant compression in the vicinity of the fault. Furthermore, the resulting mantle *S*-wave velocities decrease from values around 5.5 to 4.5 km s^{-1} towards the fault. This decrease is probably caused by serpentinization and indicates that the oceanic transform fault affects a broad region in the uppermost mantle. Conclusively, the presented method is useful for the estimation of the local *S*-wave velocity structure beneath ocean bottom seismic stations. It is easy to implement and consists of two main steps: (1) measurement of apparent *P*-wave incidence angles in different period ranges for real and synthetic data, and (2) comparison of the determined apparent *S*-wave velocities for real and synthetic data to estimate *S*-wave velocity-depth models.

Key words: Time-series analysis; Body waves; Theoretical seismology; Oceanic transform and fracture zone processes.

1 INTRODUCTION

The polarization angle of the particle motion (apparent incidence angle $\overline{\varphi}_p$) of an incoming *P* (compressional) wave at the free surface or the solid-liquid interface is the result of a superposition of the displacements of the incident *P* wave and the reflected *P* wave and *S* (shear) wave. The measured polarization of the *P* wave (i.e. apparent *P*-wave incidence angle $\overline{\varphi}_p$) therefore differs from the real incidence

© The Authors 2016. Published by Oxford University Press on behalf of The Royal Astronomical Society.

Downloaded from http://gji.oxfordjournals.org/ at GEOMAR Helmholtz-Zentrum fuer Ozeanforschung Kiel on November 23, 2016

angle φ_{p1} of the incident *P* wave (Fig. 1). Wiechert (1907) showed that for the case of the free surface, the apparent *P*-wave incidence angle $\overline{\varphi}_p$ is twice the angle of the reflected *SV* wave (vertically polarized *S* wave, φ_s). The analytical determination of the apparent *P*-wave incidence angle $\overline{\varphi}_p$ is based on the reflection coefficients at the corresponding interface (i.e. free surface or ocean bottom). Due to the influence of the water column (WC), the relation of the apparent *P*-wave incidence angle valid for the ocean bottom has to differ from the free surface relation given by Wiechert (1907).

The apparent incidence angle can be interpreted in different ways. Measurements of the apparent *P*-wave and *S*-wave incidence angles were used by Nuttli & Whitmore (1961, 1962) to determine *P*-wave velocities from *P*-waves with periods of 3–7 s and *S* waves with periods in the order of 10 s. They found *P*-wave velocities over 7 km s^{-1}. This result was interpreted by Phinney (1964) to be an indicator that the polarization is dependent on the period range used for the analysis and that for shorter periods lower velocities would be obtained. Krüger (1994) used the *P*-wave polarization to study the sedimentary structure at the Gräfenberg array in southern Germany by analysing the steepening of the P wave onset in terms of the ratio between *P*-wave and *S*-wave velocities. Whereas Svenningsen & Jacobsen (2007) and Kieling *et al.* (2011) used a progressive low-pass filtering of receiver functions (RFs) and the relation presented by Wiechert (1907) to perform an inversion for an *S*-wave velocity-depth model.

Usually, the *P*-wave polarization angle is determined by the measurement of the particle motion on the vertical (Z) and radial (R) component of a seismogram (Krüger 1994). This measurement needs a careful time window selection and data preparation, because it is influenced by the often complicated *P*-wave signal. Svenningsen & Jacobsen (2007) proposed to use (Z, R) RFs instead of the raw earthquake signal to avoid this complexity issue and to ease automatic processing. The earthquake signal is deconvolved either in time domain (Kind *et al.* 1995; Kieling *et al.* 2011) or frequency domain (Ammon 1991). This procedure transforms the *P*-wave signal into a (band limited) spike like signal on the vertical and radial component of the RF at $t = 0$. Thus, the apparent *P*-wave incidence angle can be measured by determining the amplitudes of the spike on the two components (Svenningsen & Jacobsen 2007).

Ocean bottom stations (OBSs) are sensors constructed for the deployment on the ocean floor (Webb 1998; Dahm *et al.* 2006). Often, OBS recordings have a poor signal-to-noise ratio (SNR) and suffer from high noise levels especially on the horizontal components. This results in a small number of usable event recordings for these sensors which usually operate for one year or less (Webb 1998). We increase the number of usable recordings by including P_{diff} (90°–110° epicentral distance) and PKP (140°–160°) recordings besides *P*-wave recordings (30–90°) in our analysis. Furthermore, we have to reconsider the apparent *P*-wave incidence angle relation for the free surface presented by Wiechert (1907) for the case of the ocean bottom, because the refracted P wave in the WC has an influence on the reflection coefficients of the ocean bottom. These coefficients are needed to calculate the displacements within the ocean bottom. The coefficients for the reflection and refraction at the interface between a solid and a liquid half-space were calculated for specific model parameters by Knott (1899). Zoeppritz (1919) presented an analytical calculation of the coefficients which can also be found in some textbooks (e.g. Ben-Menahem & Singh 1981). These Zoeppritz equations are also used in reflection seismic (e.g. Wang 1999b) or RF studies (Julià 2007; Kumar *et al.* 2014; Kumar 2015) to analyse impedance contrasts at interfaces.

We use the reflection coefficients to obtain a new relation which enables us to determine apparent (half-space) *S*-wave velocities from *P*-wave polarization (apparent *P*-wave incidence angle) measurements. We employ this relation together with a progressive low-pass filtering analogue to Svenningsen & Jacobsen (2007) and a quantitative modelling to obtain *S*-wave velocity-depth models.

1.1 Previous studies of oceanic *S*-wave velocity

The *S*-wave velocity structure of the oceanic crust and the upper mantle has mainly been studied by global tomography of surface waves (Romanowicz 2003; Laske *et al.* 2013) using land stations. The results of those global studies are biased by the poor data coverage in the oceans (Romanowicz 2003). Moreover, these studies employ long wavelengths for their investigation and the resolution of the gained models is therefore rather low (up to several degrees, Romanowicz 2003; Laske *et al.* 2013). If phase velocities or group velocities are used to determine *S*-wave velocity maps, several stations or arrays are needed and the obtained results reflect more the average velocity between pairs of stations than single station's estimates (Weidle & Maupin 2008; Maupin 2011; Gao & Shen 2015). Another approach to estimate the *S*-wave velocity structure of the oceanic lithosphere is the seafloor compliance inversion (Yamamoto & Torii 1986; Crawford *et al.* 1998; Webb 1998). This technique analyses the ratio of seafloor displacement to pressure loading due to infragravity waves in a very low frequency band (0.003 to 0.04 Hz, Crawford *et al.* 1998). The usage of this technique is limited, because the displacement by ocean surface waves at deep water sites is small and difficult to measure (Crawford *et al.* 1998; Webb 1998).

There have also been attempts to extract information about the shallow *S*-wave velocity structure from active seismic data (e.g. up to 300 m in Ritzwoller & Levshin (2002) and for the upper tens of metres in Nguyen *et al.* (2009)). The success of these techniques is directly related to the distance of the active source to the seafloor. The closer the source is located to the seafloor the more acoustic energy can be converted into *S*-wave energy (Ritzwoller & Levshin 2002). The inversion of these active data results in high resolution *S*-wave velocity models, but it is limited to the upper hundreds of metres beneath the seafloor. We therefore propose that by using progressive low-pass filtering (∼0.05 to 2 Hz), the analysis of *P*-wave polarization in terms of *S*-wave velocities will provide the opportunity to resolve deeper (crustal) *S*-wave velocity structures than active seismics and will give a better resolution of the crustal *S*-wave velocity structures than compliance measurements.

First, we use the reflection coefficients provided by Zoeppritz (1919) and Ben-Menahem & Singh (1981) to find a relation for the apparent P wave incidence angle at the ocean bottom analogue to the one presented by Wiechert (1907). Then, we describe the analysis of the *P*-wave polarization by progressive low-pass filtering of (Z, R) RF and the estimation of apparent *S*-wave velocities. We perform several synthetic tests to investigate the resolution of the proposed method. Finally, we apply the method to real OBS data from the Eastern Mid Atlantic Ocean and perform a quantitative modelling to determine sedimentary, crustal and mantle *S*-wave velocities and the thickness of the sediments and the oceanic crust.

2 THEORY

Considering a seismometer which measures the displacement on the seafloor, we define a local coordinate system with a vertical *z*-axis pointing upward and a horizontal *r*-axis pointing in the horizontal

Downloaded from http://gji.oxfordjournals.org/ at GEOMAR Helmholtz-Zentrum fuer Ozeanforschung Kiel on November 23, 2016

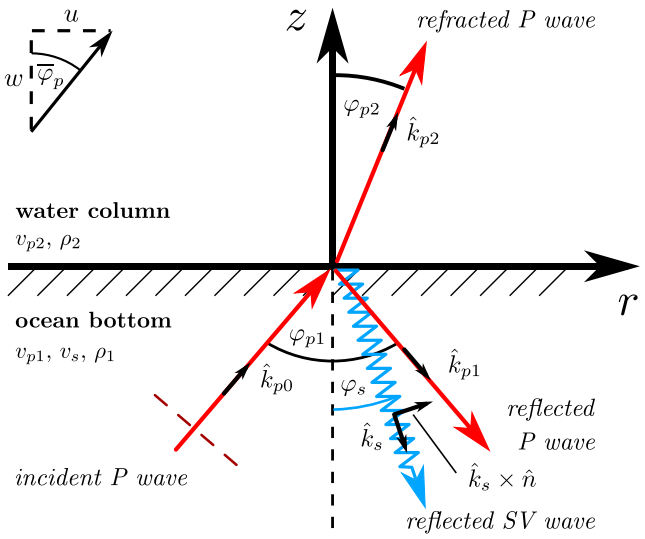

Figure 1. Polarities of *P*-waves (red) and *SV* wave (blue) at the interface between water column and ocean bottom. The incoming *P*-wave front is represented as dashed red line. The particle motions of the single wave types are shown as small black arrows. The normal of the *zr*-plane $\hat{n}$ points into the negative transverse direction. The ocean bottom has the *P*-wave velocity v_{p1}, the *S*-wave velocity v_s and the density ρ_1. The water column has the *P*-wave velocity v_{p2} and the density ρ_2. The displacements u and w are measured at the seafloor to estimate the *P*-wave polarization (apparent incidence angle, $\overline{\varphi}_p$).

propagation direction of the wave front (Fig. 1, dashed red line). The *z*-axis is thus parallel to the vertical (Z) component of the recorded seismogram and the *r*-axis is parallel to the radial (R) component. The displacement u is measured along the *r*-axis and the displacement w along the *z*-axis (Fig. 1). The tangent of the ratio of those displacements is used to estimate the *P*-wave polarization $\overline{\varphi}_p$ (apparent incidence angle, Fig. 1 and Wiechert 1907):

$$\tan\overline{\varphi}_p = \frac{u}{w}. \tag{1}$$

The displacements u and w result from the superposition of the displacements of different elastic waves at the interface between WC and ocean bottom ($z = 0$ in Fig. 1). The boundary conditions for the displacement at the interface between a fluid with low viscosity, for example, water and a solid are that the displacement normal to the interface (i.e. w) must be continuous, whereas the tangential components (i.e. u) can be discontinuous (Knott 1899; Ben-Menahem & Singh 1981; Aki & Richards 2002). Assuming the seismometer of an OBS measures the displacement of the ocean bottom, we have to consider the amplitudes of the elastic waves in the ocean bottom to obtain the *P*-wave polarization $\overline{\varphi}_p$ at the ocean floor.

In Fig. 1, the unit vectors describing the polarization direction of the incident *P*-wave ($\hat{k}_{p0}$), the reflected *P*-wave ($\hat{k}_{p1}$) and the reflected *S*-wave ($\hat{k}_s \times \hat{n}$) are presented.

$$\hat{k}_{p0} = \begin{pmatrix} \sin\varphi_{p1} \\ 0 \\ \cos\varphi_{p1} \end{pmatrix} \hat{k}_{p1} = \begin{pmatrix} \sin\varphi_{p1} \\ 0 \\ -\cos\varphi_{p1} \end{pmatrix} \hat{k}_s \times \hat{n} = \begin{pmatrix} \cos\varphi_s \\ 0 \\ \sin\varphi_s \end{pmatrix}, \tag{2}$$

where φ_{p1} and φ_s are the angles of the incident (and reflected) *P* wave, and the reflected *SV* wave, respectively and $\hat{n}$ denotes the normal of the *zr*-plane. The reflection coefficient $\acute{P}\grave{P}$ is defined as the amplitude ratio of the reflected *P* wave and the incident *P* wave and the reflection coefficient $\acute{P}\grave{S}$ is the amplitude ratio of the reflected *SV* wave and the incident *P* wave. Following Aki & Richards (2002), we use an acute accent (e.g. $\acute{P}$) to represent an upcoming wave and a grave accent (e.g. $\grave{P}$) to denote a down-going wave. Considering the reflection coefficients and eq. (2), eq. (1) can be written as:

$$\tan\overline{\varphi}_p = \frac{(1+\acute{P}\grave{P})\sin\varphi_{p1} + \acute{P}\grave{S}\cos\varphi_s}{(1-\acute{P}\grave{P})\cos\varphi_{p1} + \acute{P}\grave{S}\sin\varphi_s}. \tag{3}$$

The numerator and the denominator of eq. (3) are analogue to the displacements in *r* and *z* directions provided by Pilant (1979) and Aki & Richards (2002) for the solid-solid case, and by Ben-Menahem & Singh (1981) for the solid-liquid case. The signs of $\cos\varphi_{p1}$ and $\cos\varphi_s$ are negative in Pilant (1979) and Ben-Menahem & Singh (1981) in which the *z* axis is defined downward instead of upward as in the seismometer based definition used here (Fig. 1).

We calculated the coefficients $\acute{P}\grave{P}$ and $\acute{P}\grave{S}$ and compared them to the coefficients published by Zoeppritz (1919):

$$\acute{P}\grave{P} = \frac{1-f(1-g)}{1+f(1+g)} \tag{4}$$

$$\acute{P}\grave{S} = \frac{4\frac{v_s\rho_1}{v_{p2}\rho_2}\sin\varphi_{p1}\cos\varphi_{p2}\cos(2\varphi_s)}{1+f(1+g)} \tag{5}$$

$$\text{with:}\quad f = \frac{v_{p1}\rho_1}{v_{p2}\rho_2}\frac{\cos\varphi_{p2}\cos^2(2\varphi_s)}{\cos\varphi_{p1}} \tag{6}$$

$$g = \left(\frac{v_s}{v_{p1}}\right)^2 \frac{\sin(2\varphi_{p1})\tan(2\varphi_s)}{\cos(2\varphi_s)}. \tag{7}$$

They are similar besides that Zoeppritz (1919) provides eq. (4) with a negative sign, because his definition of the polarization direction of the reflected *P* wave ($\hat{k}_{p1}$) is opposite to the definition used here (positive in *r* and negative in *z* direction, Fig. 1). In eqs (4)–(7), v_{p1}, v_s and ρ_1 are the *P*-wave and *S*-wave velocity as well as the density of the ocean bottom, and v_{p2} and ρ_2 are the *P*-wave velocity and the density of the WC. The coefficients in eqs (4) and (5) are equivalent to the coefficients provided by Ben-Menahem & Singh (1981) for the mantle-core reflection except for the polarity of $\acute{P}\grave{S}$ which can be explained by the before mentioned differing definition of the *z* axis.

We insert eqs (4)–(7) in eq. (3) and use Snell's law

$$\frac{\sin\varphi_{p1}}{v_{p1}} = \frac{\sin\varphi_{p2}}{v_{p2}} = \frac{\sin\varphi_s}{v_s} = p \ldots \text{horizontal slowness} \tag{8}$$

to obtain the relation for the apparent *P*-wave incidence angle at the ocean bottom (see supplementary material for details of calculation):

$$\tan\overline{\varphi}_p = \tan(2\varphi_s) + \frac{\rho_2}{\rho_1}\frac{\tan\varphi_{p2}}{\cos(2\varphi_s)}. \tag{9}$$

The new eq. (9) has two terms, the first term equals the well-known relation for the free surface of a solid half-space (Wiechert 1907) and the second term describes the influence of the WC on the apparent *P*-wave incidence angle.

Downloaded from http://gji.oxfordjournals.org/ at GEOMAR Helmholtz-Zentrum fuer Ozeanforschung Kiel on November 23, 2016

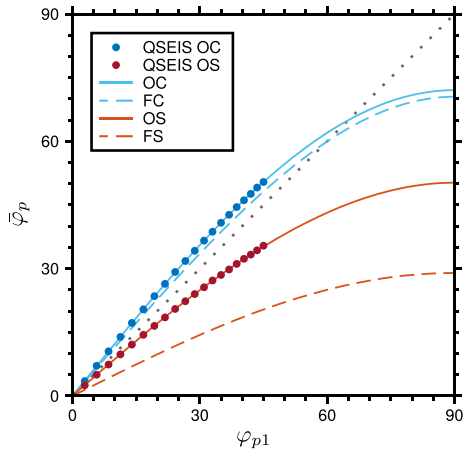

Figure 2. Comparison of eq. (9) and Wiechert formula ($\overline{\varphi}_p = 2\varphi_s$). The theoretical apparent *P*-wave incidence angle $\overline{\varphi}_p$ on the ocean floor if the *P*-wave incidence angle φ_{p1} is given are shown as solid lines. The $\overline{\varphi}_p$ at the free surface if φ_{p1} is given are shown as dashed lines. The values for an oceanic crust (OC: water layer/ crust, FC: free-surface/ crust, Table 1) are shown in blue and the values for a sediment (OS: water layer/ sediment, FS: free-surface/ sediment, Table 1) in red. The measured apparent *P*-wave incidence angles from synthetic seismograms (QSEIS) are presented as circles for the OC model (blue) and the OS model (red).

Using Snell's law (eq. 8), eq. (9) is re-written as function of the horizontal slowness p (see supplementary material for details of calculation):

$$\tan\overline{\varphi}_p = \frac{p\left(\frac{\rho_2}{v_s^2} + 2\rho_1\sqrt{\frac{1}{v_s^2}-p^2}\sqrt{\frac{1}{v_{p2}^2}-p^2}\right)}{\rho_1\sqrt{\frac{1}{v_{p2}^2}-p^2}\left(\frac{1}{v_s^2}-2p^2\right)}. \tag{10}$$

Eq. (10) shows that the apparent *P*-wave incidence angle $\overline{\varphi}_p$ is independent of the *P*-wave velocity v_{p1} of the ocean bottom. In Fig. 2, we present a comparison between $\overline{\varphi}_p$ for the ocean bottom and the free surface. It becomes clear that the apparent *P*-wave incidence angles differ especially for the water/sediment contrast. Moreover, if apparent *S*-wave velocities are estimated at the ocean bottom using the free surface relation, the obtained velocities will be higher than the true values (compare eq. 10).

3 METHODOLOGY

The estimation of apparent *P*-wave incidence angles ($\overline{\varphi}_p$) can be done by using hodographs of the *P*-wave particle motion (Krüger 1994). The *P*-wave train can be rather complex because of the influence of the source time function and the source-to-receiver wave propagation. The analysis of the particle motion therefore requires a careful data preparation and time window selection. The processing is eased by employing RFs for which the R component is deconvolved with the Z component (Svenningsen & Jacobsen 2007). By this procedure, the *P*-wave signal turns into a zero-phase (band-limited) spike which arrives at time $t = 0$ on the vertical (Z_{RF}) and radial (R_{RF}) component. We perform the deconvolution in time domain by using a Wiener filter (Kind *et al.* 1995; Kieling *et al.* 2011). The apparent *P*-wave incidence angle can be estimated by measuring the amplitudes at $t = 0$ on Z_{RF} and R_{RF} (Svenningsen & Jacobsen 2007). On R_{RF}, additionally a series of *P* to *S* converted signals become visible after the projection of the direct *P* spike signal.

Table 1. Model parameters for standard values of water column (WC), sediment (SD), normal oceanic crust (NOC), oceanic crust with 10 per cent reduced velocities and density (ROC), normal mantle (NM) and mantle with 10 per cent reduced velocities and density (RM). We give the *P*-wave velocity v_p, the *S*-wave velocity v_s and the density ρ.

Medium	v_p [km s^{-1}]	v_s [km s^{-1}]	ρ [g cm^{-3}]
WC	1.500	0.000	1.000
SD	2.000	0.500	2.000
NOC	6.500	3.750	2.700
ROC	5.850	3.375	2.430
NM	8.120	4.510	3.340
RM	7.308	4.059	3.006

The seismic velocities obtained by analysing the *P*-wave polarization (apparent *P*-wave incidence angle, $\overline{\varphi}_p$) are dependent on the used period range (Haskell 1962; Phinney 1964). For longer periods (~5–10 s), the obtained velocities are typical for the Earth's mantle (Nuttli & Whitmore 1961, 1962). If shorter periods are used for the measurement of the *P*-wave polarization $\overline{\varphi}_p$, the estimated velocities will be similar to crustal velocities (Phinney 1964; Svenningsen & Jacobsen 2007). This behaviour can be used to obtain velocity-depth profiles (Svenningsen & Jacobsen 2007). In order to analyse the apparent *P*-wave incidence angles, we apply a set of different low pass filters to the (Z, R) RF before estimating the angles (Svenningsen & Jacobsen 2007). We use Butterworth low-pass filters of second order which are applied forwards and backwards in order to get zero phase filters (Scherbaum 2001). The corner periods of the filters are chosen to be logarithmically distributed as suggested by Svenningsen & Jacobsen (2007).

The (Z, R) RFs are calculated and filtered with L low pass filters for N events. After the filtering, the apparent *P*-wave incidence angles $\overline{\varphi}_{p,n}^{obs}(T_l)$ are measured for each corner period T_l at time $t = 0$ of the filtered (Z, R) RFs. A misfit function m can be formed which compares the measured apparent *P*-wave incidence angles $\overline{\varphi}_{p,n}^{obs}(T_l)$ for N different events with their calculated theoretical equivalent $\overline{\varphi}_p^{theo}$ using eq. (10) for each corner period T_l:

$$m(v_s, \rho_1, T_l) = \frac{1}{\sum_{n=1}^{N} w_n} \cdot \sum_{n=1}^{N} (|D(T_l, v_s, \rho_1, p_n)| \cdot w_n) \tag{11}$$

with

$$D(T_l, v_s, \rho_1, p_n) = \tan\overline{\varphi}_{p,n}^{obs}(T_l) - \tan\overline{\varphi}_p^{theo}(v_s, \rho_1, p_n).$$

The weights w_n are chosen based on data quality. Standard values (Table 1) are used for the *P*-wave velocity v_{p2} and density ρ_2 of the WC to calculate the theoretical angle $\overline{\varphi}_p^{theo}$ (eq. 10). The horizontal slowness p_n for each event n is calculated for global velocity models (AK135, Kennett *et al.* 1995). The remaining unknowns in eq. (11) are the *S*-wave velocity v_s and the density ρ_1 of the ocean bottom. In the following section, we perform synthetic tests to analyse the dependency of the apparent incidence angle on the *S*-wave velocity v_s and the density ρ_1, as well as its behaviour in dependence on the used corner period T_l for multilayered models.

4 SYNTHETIC TESTS

In this section, we want to investigate typical structures of the ocean bottom by calculating synthetic data for different oceanic layered velocity models with a full wave field reflectivity method (QSEIS;

Downloaded from http://gji.oxfordjournals.org/ at GEOMAR Helmholtz-Zentrum fuer Ozeanforschung Kiel on November 23, 2016

Table 2. Model description for synthetic tests (regional case). All models include a water column (WC) of 5.05 km (layer 1). Layer thickness for sediment (SD), normal oceanic crust (NOC) and normal mantle (NM) (for model parameters, see Table 1). The source depth is given in kilometres b.s.f.

Model	Layer 2	Half-space	Source depth [km b.s.f.]
OC	–	NOC	100
OS	–	SD	100
N	7 km NOC	NM	100
S100C	0.1 km SD	NOC	100
S200C	0.2 km SD	NOC	100
S300C	0.3 km SD	NOC	100
S400C	0.4 km SD	NOC	100
S600C	0.6 km SD	NOC	100
S800C	0.8 km SD	NOC	100
S1000C	1 km SD	NOC	100

Table 3. Description of models at the receiver site for synthetic tests (teleseismic case). All models include a water column (WC) of 5.05 km (layer 1), PREM below 155.05 km and continental PREM for the source site (Supporting Information Fig. S1). Layer thickness for normal oceanic crust (NOC), oceanic crust with 10 per cent reduced velocities and density (ROC), normal mantle (NM) and mantle with 10 per cent reduced velocities and density (RM) (for model parameters, see Table 1).

Model	Layer 2	Layer 3	Layer 4	Layer 5
CM-REF	7 km NOC	143 km NM	–	–
CI	1 km ROC	6 km NOC	143 km NM	–
CII	3 km NOC	1 km ROC	3 km NOC	143 km NM
CIII	6 km NOC	1 km ROC	143 km NM	–
MI-50	7 km NOC	50 km RM	93 km NM	–
MII-50	7 km NOC	3 km NM	50 km RM	90 km NM
MIII-50	7 km NOC	13 km NM	50 km RM	80 km NM
MIV-50	7 km NOC	23 km NM	50 km RM	70 km NM
MV-50	7 km NOC	43 km NM	50 km RM	50 km NM
MVI-50	7 km NOC	93 km NM	50 km RM	–
MIV-1	7 km NOC	23 km NM	1 km RM	119 km NM
MIV-5	7 km NOC	23 km NM	5 km RM	115 km NM
MIV-10	7 km NOC	23 km NM	10 km RM	110 km NM
MIV-20	7 km NOC	23 km NM	20 km RM	100 km NM
MIV-100	7 km NOC	23 km NM	100 km RM	20 km NM

Wang 1999a) using the model parameters listed in Table 1. We use a normalized squared half-sinus function with a length of 0.5 s which has a flat spectra below 2 Hz as source time function. The reflectivity method is not able to model a liquid layer with an *S*-wave velocity $v_s = 0$ km s^{-1}, instead we use a very soft solid layer for which the *P*- to *S*-wave velocity ratio is 1000 as suggested by Müller (1985). The sensor depth is chosen to be 1 m below seafloor (b.s.f.).

In order to save computation time and to obtain high-frequency synthetic data, we first simulate deep regional events (100 km depth) instead of teleseismic global events. The models for the regional case are listed in Table 2. In a first step, we test the accuracy of QSEIS against the theoretical expression in eq. (10) using two half-space models. Afterwards, we add one layer to investigate the depth resolution of the proposed method. In a third step, we simulate teleseismic global events with a low sampling frequency (8 Hz) to investigate the influence of water depth and a low velocity layer (LVL; Table 3). For the synthetic tests in this section, we set all weights (w_n in eq. 11) to one.

4.1 Half-space *S*-wave velocity

The first deep regional source models (model OC and OS, Table 2) consist of one layer over a half-space. Model OC includes a WC (Table 1) and a normal oceanic crust (NOC, Table 1) half-space, and model OS a WC and a sediment (SD, Table 1) half-space. An explosion source is located at 100 km b.s.f. and the receivers are placed in 5 to 100 km epicentral distance with 5 km inter-station spacing. This setting corresponds to slowness values of 0.9 s/° to 12.1 s/° for the OC model and 2.8 s/° to 39.3 s/° for the OS model, respectively. The sampling rate is 100 Hz.

The apparent *P*-wave incidence angles $\overline{\varphi}^{\text{obs}}_{p,n}$ are determined by measuring the polarization for the P wave of each synthetic event within a 1 s time window for unfiltered data on the Z and R components (circles in Fig. 2). By directly comparing, we find a good agreement between measured and theoretical angles for the OC model (solid blue line and blue circles in Fig. 2) and the OS model (solid red line and red circles in Fig. 2). This shows that the apparent *P*-wave incidence angles obtained from synthetic data (QSEIS) are similar to the values estimated with our theoretical expression in eq. (10).

Furthermore, we test the dependency of the misfit $m(v_s, \rho_1)$ (eq. 11) on the *S*-wave velocity v_s and the density ρ_1 by using the measured apparent *P*-wave incidence angles of the OC model.

The misfit is calculated based on a grid search over *S*-wave velocity v_s (0.1–9.0 km s^{-1} in 0.1 km s^{-1} steps) and density ρ_1 (1.0-6.0 g cm^{-3} in 0.1 g cm^{-3} steps). The result shows that the dependency of the misfit function $m(v_s, \rho_1)$ and therefore of the apparent *P*-wave incidence angle on the *S*-wave velocity v_s is much stronger than on the density ρ_1 (Fig. 3). By searching for the minimum in the misfit for each tested density value ρ_1, an *S*-wave velocity range (black dashed lines in Fig. 3) is determined, for which a median (red line in Fig. 3) is estimated. In the presented case, the median of the apparent *S*-wave velocity $v_{s,\text{app}}$ is 3.8 km s^{-1} and its range is 3.4–3.9 km s^{-1}. If we do not put any constrains on the density for a grid search with a *S*-wave velocity step size of 0.1 km s^{-1}, the

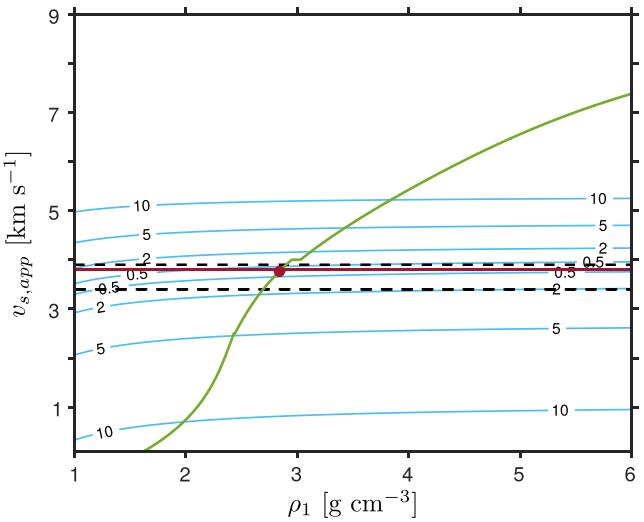

Figure 3. Misfit function $m(v_s, \rho_1)$ calculated by eq. (11) is shown as blue contours over *S*-wave velocity v_s and density ρ_1 of the ocean bottom for the OC model with WC over NOC. The range in the apparent *S*-wave velocity $v_{s,\text{app}}$ estimated by the minimum of the misfit for each tested density is indicated by black dashed lines. The median of the apparent *S*-wave velocity $v_{s,\text{app}}$ for all tested densities is shown in red. The relation $\rho_1(v_s)$ is presented in green and the estimated $v_{s,\text{app}}$ for the root search is depicted as red circle.

Downloaded from http://gji.oxfordjournals.org/ at GEOMAR Helmholtz-Zentrum fuer Ozeanforschung Kiel on November 23, 2016

obtained median $v_{s,app}$=3.8 km s^{-1} is a good estimate of the *S*-wave velocity used in the model (v_s = 3.75 km s^{-1}).

Instead of a grid search, we can perform a root search to estimate $v_{s,app}$ by assuming a relation between the density ρ_1 and the *S*-wave velocity v_s. There are well known empirically derived relations between the density ρ_x and the *P*-wave velocity v_{px} (Brocher 2005, eq. 12), for v_{px} in km s^{-1} and ρ_x in g cm^{-3}).

$$\rho_x = 1.6612 \cdot v_{px} - 0.4721 \cdot v_{px}^2 + 0.0671 \cdot v_{px}^3 - 0.0043 \cdot v_{px}^4 + 0.000106 \cdot v_{px}^5. \quad (12)$$

To obtain $\rho_1(v_s)$, we have to assume $v_p(v_s)$. For *S*-wave velocities up to 2.5 km s^{-1}, the mud-rock line ($v_p = 1.16 \cdot v_s + 1.36$, Castagna *et al.* 1985) serves quite well. For larger *S*-wave velocities, a constant v_p/v_s ratio could be assumed ($v_p/v_s = \sqrt{3}$ for 2.5 km s^{-1} < v_s ≤ 4.0 km s^{-1} and v_p/v_s = 1.8 for v_s > 4.0 km s^{-1}). By using the assumed relation $\rho_1(v_s)$ (green line in Fig. 3) in eq. (11), the minimum misfit $m(v_s, \rho_1(v_s))$ for the OC model is estimated at $v_{s,app}$ = 3.76 km s^{-1} (red circle in Fig. 3) for an *S*-wave velocity step size of 0.005 km s^{-1}. This velocity is in good agreement with the used model parameter (v_s = 3.75 km s^{-1}) and similar to the median $v_{s,app}$ obtained by the grid search with a coarser step size.

In conclusion, the weak dependency of the misfit function $m(v_s, \rho_1)$ (i.e. the apparent *P*-wave incidence angle) on the density shows that we could hardly resolve densities with the presented method. We therefore will neglect the weak influence of the density in the further processing.

In the next section, we analyse the behaviour of $v_{s,app}$ with the period T_l for a layered model and compare the results obtained by estimating the median $v_{s,app}$ with the grid search and by determining $v_{s,app}$ using the root search. Both approaches have proved to give good estimates of the true half-space *S*-wave velocity.

4.2 Depth resolution

We use several synthetic models to test the depth resolution of the method. All models presented in Figs 4 and 5 include a 5.05 km thick WC which is given by CRUST 1.0 for the area of the OBS deployment (Supporting Information Fig. S1; Laske *et al.* 2013). The angles in Table 4 give the direction the ray travels within the half-space and are measured towards the normal of the layer interface (i.e. against vertical). The associated slowness values are also given in Table 4. The vertical component of the synthetic data (100 Hz) is used to create a Wiener filter, choosing a 5 s time window starting at the *P* onset. The filter is used to deconvolve the vertical and radial components in order to estimate (Z, R) RF for the analysis. The RF are filtered with a set of low pass filters with *L* corner periods T_l which are logarithmically distributed (0.5 s to 64 s, 8 filters per octave). The apparent *P*-wave incidence angles are estimated from the amplitudes on Z_{RF} and R_{RF} at time $t = 0$ (relative to deconvolved *P* spike on Z_{RF}).

We test model N which consists of 7 km NOC (Table 1) over a normal mantle (NM, Table 1) half-space b.s.f. We obtain $m(v_s, \rho_1, T_l)$ and $m(v_s, \rho_1(v_s), T_l)$ for the estimated apparent *P*-wave incidence angles and different periods T_l. The minima of misfit $m(v_s, \rho_1, T_l)$ are determined for each density ρ_1. We obtain the median $v_{s,app}$ for each period T_l and estimate the roots of $m(v_s, \rho_1(v_s), T_l)$ to get the $v_{s,app}$ profiles (black and grey solid line in Fig. 4). To show the variability of the results for slowness values typical for P and P_{diff} (4–9 s/°, ∼30°–110° epicentral distance) and PKP_{df} (1–2 s/°, ∼140°–160° epicentral distance), we included the median $v_{s,app}$ profiles for synthetic event 1 (1.19 s/°, dashed yellow line in Fig. 4), synthetic event 4 (4.68 s/°, dash-dot red line in Fig. 4) and synthetic event 8 (8.80 s/°, dashed red line in Fig. 4).

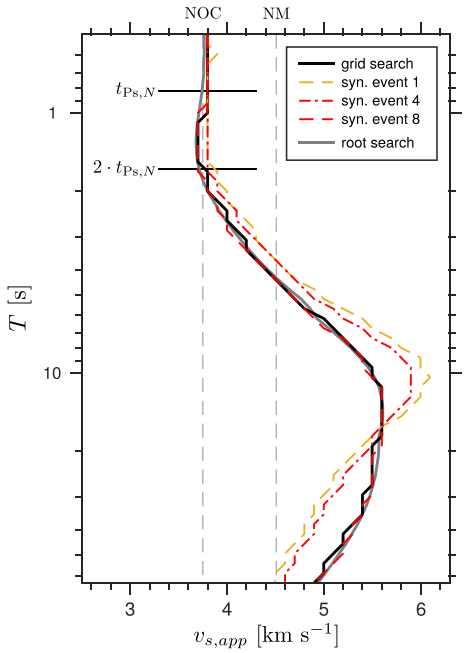

Figure 4. Synthetic test for model N (7 km NOC over NM half-space below seafloor, Tables 1 and 2). The *S*-wave velocities used in the model are marked by dashed light grey lines. The median $v_{s,app}$ profiles obtained for synthetic event 1 (dashed yellow, Table 4), synthetic event 4 (dash-dot red, Table 4) and synthetic event 8 (dashed red, Table 4) are shown. The median $v_{s,app}$ profile obtained from the total misfit function of all events (grid search, eq. 11) is shown in black. The $v_{s,app}$ profile estimated using the root search is presented in grey.

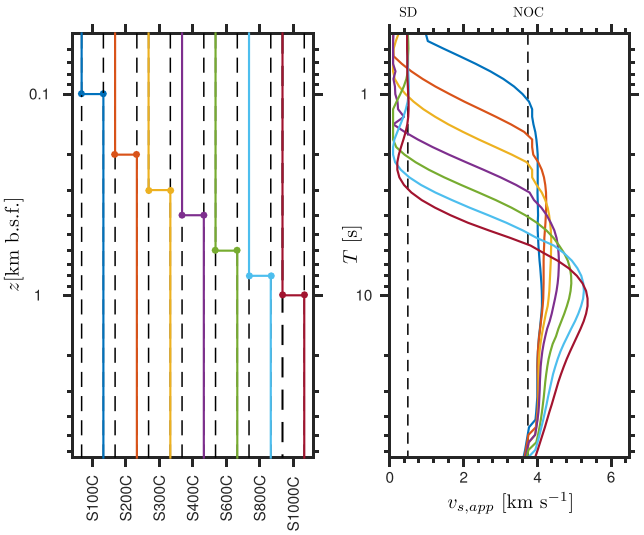

Figure 5. Synthetic tests for two layers (including WC and SD) over NOC half-space. Detailed model description can be found in Table 2 and used parameters in Table 1. Left panel shows used velocity models for depth below seafloor (b.s.f.). Right panel shows estimated $v_{s,app}$ profiles with corner period *T*.

The $v_{s,app}$ profiles obtained by the grid search and the root search agree very well. The only difference is the smoother appearance of the root search profile due to the smaller step size in v_s (0.005 km s^{-1} compared to 0.1 km s^{-1}). Besides this, the overall appearance of both profiles is identical.

Downloaded from http://gji.oxfordjournals.org/ at GEOMAR Helmholtz-Zentrum fuer Ozeanforschung Kiel on November 23, 2016

Table 4. Take-off angles and slowness values used for models in Table 2 (regional case). The values are given for a half-space consisting of either normal oceanic crust (NOC) or normal mantle (NM).

Event	Take-off angle	Slowness [s °$^{-1}$] NOC	NM
1	5	1.49	1.19
2	10	2.97	2.38
3	15	4.43	3.54
4	20	5.85	4.68
5	25	7.23	5.79
6	30	8.55	6.85
7	35	9.81	7.85
8	40	11.00	8.80
9	45	12.10	9.68

The $v_{s,\mathrm{app}}$ profiles show the velocity of the upper layer for periods up to ~2 s. For this period range, all obtained $v_{s,\mathrm{app}}$ profiles agree very well. The kinks of the profiles at which they start to diverge from the *S*-wave velocity of the upper layer are approximately at $2 \cdot t_{Ps}$ which is twice the delay time of the Ps conversion for a slowness of 6.36 s/° (Fig. 4). For longer periods, the $v_{s,\mathrm{app}}$ profiles of model N bump ('overshoot') before they converge towards the velocity of the half-space (Fig. 4). This effect was also described by Svenningsen & Jacobsen (2007) and was interpreted to be related to the effect of crustal multiples on the filtered RFs for longer periods. Furthermore, we find that for smaller slowness values (e.g. 1.19 s/°, dashed yellow line in Fig. 4) the bump in the $v_{s,\mathrm{app}}$ is larger than for larger slowness values (e.g. 8.80 s/°, dashed red line in Fig. 4), but the profile with the smaller slowness value converges faster towards the half-space *S*-wave velocity. This effect can be explained by shorter delay times of crustal multiples for smaller slowness values.

Due to the agreement of the $v_{s,\mathrm{app}}$ profiles obtained by grid search and root search, we decide to present only the $v_{s,\mathrm{app}}$ profiles obtained by the root search for the following comparison of the different tested models for a better visibility of the behaviour of the different profiles. In Fig. 5, we show the results for a test of the influence of the upper solid layer thickness on the appearance of the $v_{s,\mathrm{app}}$ profiles. The models named S100C to S1000C consist of a WC and a sediment (SD) layer of thickness 100 m to 1000 m over an NOC half-space (Tables 1 and 2). The effect of 'overshooting', described for model N in Fig. 4, is also visible for the SD-NOC models. The bump in the $v_{s,\mathrm{app}}$ profile is shifted to longer periods for thicker layers, and also increases in velocity for larger thicknesses (Fig. 5). For S100C, the profile reaches a velocity of 4.13 km s^{-1}, whereas for model S1000C, the maximum velocity lies at 5.365 km s^{-1} (Fig. 5).

In conclusion, the overall appearance of the $v_{s,\mathrm{app}}$ profiles for a model with a solid layer over half-space b.s.f. is determined by the *S*-wave velocity of the upper solid layer for short periods and the *S*-wave velocity of the half-space for longer periods. The thicker the upper solid layer the longer the period and the larger the maximum $v_{s,\mathrm{app}}$ of the 'overshooting' bump in the $v_{s,\mathrm{app}}$ profile get.

4.3 Influence of water depth

For the teleseismic tests presented in Figs 6 and 7, we take advantage of the ability of QSEIS to use different source and receiver site models to calculate synthetic body waves for teleseismic distances. We choose continental PREM (Supporting Information Fig. S1; Dziewonski & Anderson 1981) on the source site and utilize different receiver site models for depths above 155.05 km (Table 3). We choose a double couple with a dip of 45°, a rake of 90° and a strike of 0° at 15 km depth as source. The source is located at a back azimuth of 69° in a distance of 47.6° (p = 7.78 s/°) which corresponds to the values for event #4 of the analysed real data (Table 5). The synthetic data are sampled with 8 Hz in order to minimize computation time. For the calculation of (Z, R) RF, we employ a Wiener filter which is estimated by using the vertical component of the synthetic seismograms and a 80 s time window starting at the *P* onset.

We create a reference model (CM-REF, Table 3) with a 5.05 km thick WC, a 7 km thick NOC and an NM layer on the receiver site

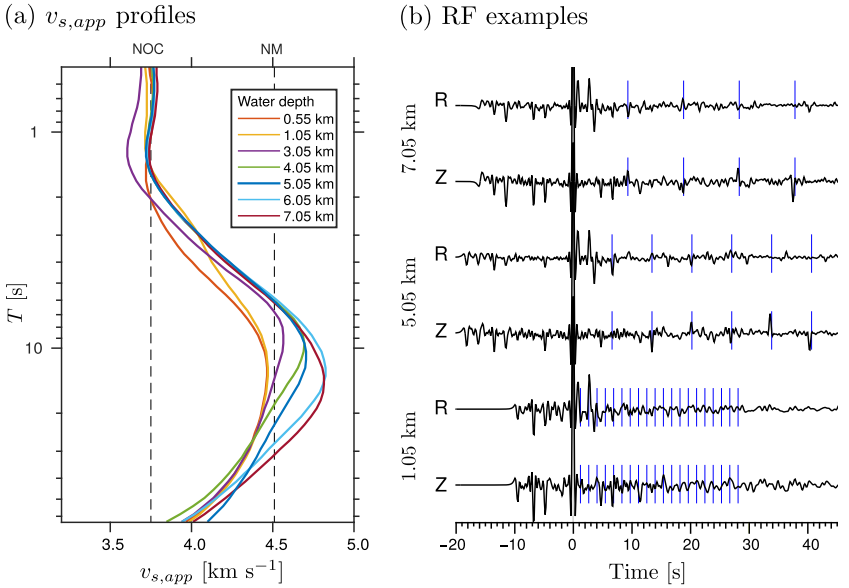

Figure 6. (a) Estimated $v_{s,\mathrm{app}}$ profiles with corner period T for synthetic tests for two layers (including WC) over oceanic PREM. Each model contains a 7 km thick layer of NOC and an NM up to a depth of 155.05 km. The water depth varies from 0.55 to 7.05 km. (b) Example RF for water depths 1.05, 5.05 and 7.05 km. The arrival times of the water multiples for each corresponding water depth are indicated by blue lines.

Downloaded from http://gji.oxfordjournals.org/ at GEOMAR Helmholtz-Zentrum fuer Ozeanforschung Kiel on November 23, 2016

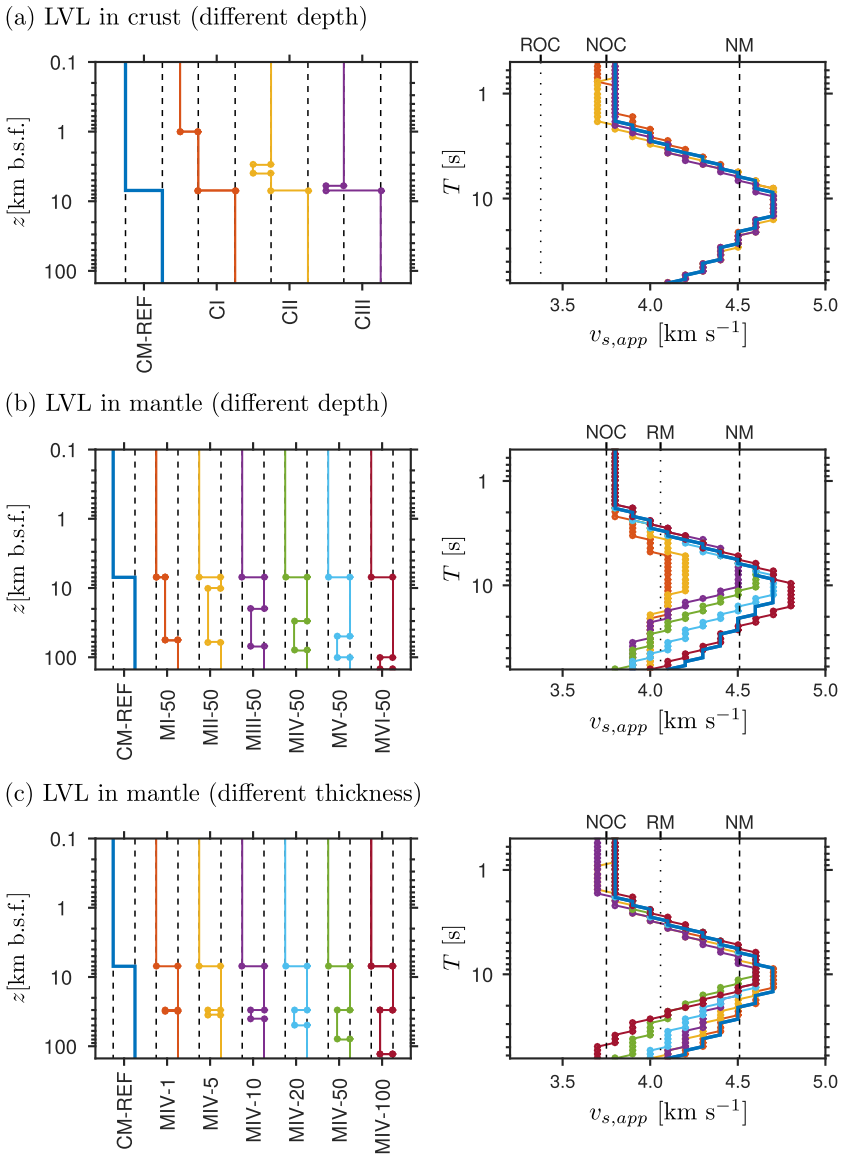

Figure 7. Synthetic test for three to five layers (including WC) over PREM. Detailed model description can be found in Table 3 and used parameters in Table 1. Left column shows used velocity models with depth below seafloor (b.s.f.). Right column shows estimated $v_{s,\mathrm{app}}$ profiles with corner period T for models in left panel. *S*-wave velocity of NOC and NM used for forward calculation are given by dashed lines. The velocity of the LVL introduced in the model is indicated by a dotted line. (a) Models and $v_{s,\mathrm{app}}$ profiles for a 1 km thick LVL at different depths in the crust. (b) Models and $v_{s,\mathrm{app}}$ profiles for a 50 km thick LVL at different depths in the mantle. (c) Models and $v_{s,\mathrm{app}}$ profiles for an LVL with different thickness at a depth of 30 km b.s.f. in the mantle.

Table 5. Events used for the *P*-wave polarization analysis, origin time, hypocentre location and moment magnitude M_w from the NEIC catalogue (earthquake.usgs.gov), Δ is the epicentral distance and p is the horizontal slowness as calculated from the AK135 traveltime tables (rses.anu.edu.au/seismology/ak135).

#	Origin time		Lat.	Lon.	Depth	M_w	p	Δ
	[dd.mm.yyyy	hh:mm:ss]	[°]	[°]	[km]		[s °$^{-1}$]	[°]
1	24.08.2011	17:46:11	−7.64	−74.53	147.0	7.0	6.14	59.0
2	02.09.2011	10:55:53	52.17	−171.71	32.0	6.9	4.85	86.9
3	02.09.2011	13:47:09	−28.40	−63.03	578.9	6.7	5.32	78.5
4	23.10.2011	10:41:23	38.72	43.51	18.0	7.1	7.78	47.6
5	22.11.2011	18:48:16	−15.36	−65.09	549.9	6.6	6.00	69.1
6	27.12.2011	15:21:56	51.84	95.91	15.0	6.6	5.90	73.5
7	26.02.2012	06:17:19	51.71	95.99	12.0	6.7	5.88	73.6
8	20.03.2012	18:02:47	16.49	−98.23	20.0	7.4	5.98	72.1
9	11.04.2012	08:38:36	2.33	93.06	20.0	8.6	4.44	105.2
10	11.04.2012	22:55:10	18.23	−102.69	20.0	6.5	5.81	74.6
11	17.04.2012	07:13:49	−5.46	147.12	198.0	6.8	1.77	144.7

Downloaded from http://gji.oxfordjournals.org/ at GEOMAR Helmholtz-Zentrum fuer Ozeanforschung Kiel on November 23, 2016

for the comparison of the estimated $v_{s,\mathrm{app}}$ profiles of the models with varied water depth and those including an LVL in either crust or mantle. The reference model is depicted with a solid blue line in Figs 6(a) and 7.

Fig. 6 shows the influence of the water depth on the appearance of the *S*-wave velocity profiles. For this test, we create receiver site models including a WC with a thickness from 0.55 to 7.05 km. The models consist of a 7 km thick NOC and a NM (Table 1) which extends to a total depth of 155.05 km where PREM takes over. It is visible that the overall appearance of the profiles is similar (Fig. 6a). All profiles have velocities similar to the NOC for periods shorter than 2 s. For longer periods, all profiles show a bump in velocity. The maximum in velocity is similar or larger than the velocity of the NM and increases for larger water depth. The decrease of $v_{s,\mathrm{app}}$ below NM velocities at longer periods is probably related to the additional (long period) phases present in the global case (e.g. W phase, Kanamori 1993) and/or the possible incomplete deconvolution of the P wave signal at these periods which depends on the Wiener filter parameters (Supporting Information Fig. S3).

The behaviour of the profiles can be explained by the influence of the water multiples which is directly related to their traveltimes. The thinner the water layer the more water multiples arrive in a shorter time window, for example, for 0.55 km the traveltime of a water multiple is ∼0.73 s and for 7.05 km ∼9.4 s ($v_{p,\mathrm{WC}} = 1.5$ km s^{-1} and $p = 7.78$ s/°, Fig. 6b). The more water multiples arrive in a shorter time window the more the signal of the direct *P*-wave gets distorted and this has a direct influence on the Wiener filter estimation for the deconvolution. This is visible in Fig. 6(b) in which the RF for water depths of 5.05 km and 7.05 km show a series of regular spaced positive and negative spikes on Z_{RF} which are expected if the direct *P*-wave is properly deconvolved. For a water depth of 1.05 km, no such spike series is observed.

Nevertheless, the water depth has only a minor influence on the appearance of the $v_{s,\mathrm{app}}$ profiles at least for the deep ocean, but a removal of the water multiples (Osen *et al.* 1999; Thorwart & Dahm 2005) before deconvolution might be useful for shallow water depths to prevent influences by wave form distortions.

4.4 Influence of LVL

We test the ability of our method to detect a LVL in different depths in either crust or mantle (Fig. 7). All models have again a 5.05 km thick WC as is given by CRUST 1.0 for the area of the deployment (Supporting Information Fig. S1; Laske *et al.* 2013). The first three models in Fig. 7(a) (CI, CII, CIII, Table 3) consist of a normal oceanic crust (NOC) with a 1 km thick layer of 10 per cent reduced crustal velocities and density (ROC) in three different depths below seafloor (0, 3 and 6 km), and a normal mantle (NM) above PREM. In Fig. 7(a), the estimated $v_{s,\mathrm{app}}$ profiles of the three models are quite similar in appearance. For model CI (orange profile in Fig. 7a), we find lower velocities for the shorter periods (<0.8 s) compared to the reference model CM-REF (blue profile in Fig. 7a). Model CII (yellow profile in Fig. 7a) has lower velocities from ∼0.7 to ∼2 s compared to the reference model. This appearance might also be explained with a model consisting of two solid layers over PREM b.s.f. with a lower crustal velocity than the reference model CM-REF. The last model CIII (purple profile in Fig. 7a) shows nearly the same appearance as the reference model CM-REF.

The next six receiver site models (MI-50, MII-50, MIII-50, MIV-50, MV-50, MVI-50, Table 3 and Fig. 7b) consist of an NOC and an NM with a 50 km thick layer of 10 per cent reduced mantle velocities and density (RM) in six different depths below seafloor (7, 10, 20, 30, 50 and 100 km). In Fig. 7(b), all profiles show a velocity of ∼3.75 km s^{-1} for periods shorter than ∼2 s which corresponds very well to the *S*-wave velocity of the NOC. The $v_{s,\mathrm{app}}$ profiles for model MI-50 and MII-50 (orange and yellow profile) significantly differ from the reference model (blue profile) for longer periods (>2 s). Both profiles show a bump in velocity, which has a maximum velocity similar to the *S*-wave velocity of the RM. Neither the profile of MI-50 nor MII-50 show velocities comparable to the NM *S*-wave velocity. The profile of model MII-50 behaves in a similar way like the profile of the model MI-50. This indicates that the 3 km thick layer of NM in model MII-50 has only small influence on the appearance of the estimated $v_{s,\mathrm{app}}$ profile. The maximum velocity of the model MII-50 is slightly increased compared to the MI-50 profile. This effect might also be explained with a model similar to MI-50 but with a faster or thicker layer than the 50 km RM.

The other models in Fig. 7(b) (MIII-50, MIV-50, MV-50 and MVI-50) show a clear bump in their $v_{s,\mathrm{app}}$ profiles. Furthermore, their profiles are nearly identical to the CM-REF profile for periods shorter than ∼5.6 s. The bump in velocity increases from 4.535 km s^{-1} to 4.8 km s^{-1} with the thickness of the upper NM layer (13 km to 93 km). Furthermore, its maximum lies at longer periods the deeper the location of the LVL. The velocities at periods longer than 16 s increase with the depth of the LVL. Despite a larger maximum velocity, the MVI-50 profile has a similar appearance as the CM-REF profile. This indicates a possible trade-off between the depth of the LVL and the uppermost mantle velocity. It might therefore be explained by a model with a higher mantle velocity and no LVL if this would be observed for real (noisy) data (Supporting Information Fig. S2).

At last, we tested the influence of a LVL in the mantle at a depth of 30 km b.s.f. for different layer thickness (1, 5, 10, 20, 50 and 100 km; models MIV-1, MIV-5, MIV-10, MIV-20, MIV-50, MIV-100, Table 3 and Fig. 7c). The appearance of all tested models in Fig. 7(c) is similar to the models MIII-50, MIV-50, MV-50 and MVI-50 discussed before. All profiles show a similar behaviour to the reference model CM-REF for periods shorter than ∼5.6 s. The appearance of the bump in velocity differs. For the models MIV-1 and MIV-5, the profiles are nearly identical to the reference model CM-REF. The profiles of the other four models (MIV-10, MIV-20, MIV-50 and MIV-100) mainly differ in the decrease in velocity with increasing thickness of the LVL for periods longer than ∼ 12 s (Fig. 7c).

In conclusion, a thin crustal LVL can be detected in the upper and middle crust, but not in the lower crust (Fig. 7a). A thin fast velocity layer or LVL in the uppermost mantle has only minor influence on the $v_{s,\mathrm{app}}$ profile. A clear influence on the $v_{s,\mathrm{app}}$ profile is visible for thicker (>10 km) fast and LVL above ∼50 km b.s.f.

4.5 Summary of synthetic tests

We conclude that the overall appearance of the $v_{s,\mathrm{app}}$ profile gives an indication of the number of layers which should be used to model the profile. The method is able to resolve either an increase or a decrease in the *S*-wave velocity (e.g. Figs 4 and 7) and it is sensitive to the thickness of the layers (e.g. Figs 5 and 7). Furthermore, we find that the water depth has only a minor influence on the appearance of the $v_{s,\mathrm{app}}$ profile (Fig. 6). A 1 km thick LVL with 10 per cent reduced crustal velocities and densities is detectable in the upper and middle

Downloaded from http://gji.oxfordjournals.org/ at GEOMAR Helmholtz-Zentrum fuer Ozeanforschung Kiel on November 23, 2016

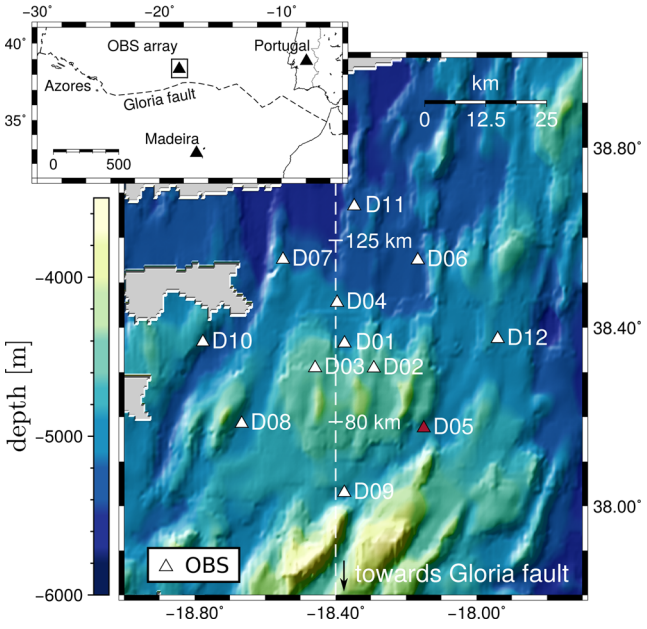

Figure 8. Layout and location of the OBS array. The bathymetry (EMEPC, Task Group for the Extension of the Continental Shelf) is indicated by the colour. The OBS positions are marked with triangles. Station D05 had two clamped components and is not used in the analysis. The distance to the Gloria fault along an N-S profile is given by the white line. The location of the OBS array and the Eurasian–African plate boundary (Gloria Fault, Bird 2003) is shown on the inset map.

crust (0–3 km b.s.f., model CI and CII), but it has only a minor influence on the appearance of the $v_{s,\mathrm{app}}$ profile if it is located in the lower crust (7 km b.s.f., model CIII). A small influence on the $v_{s,\mathrm{app}}$ profiles is also observable for thin (<10 km) fast velocity layers (e.g. MII-50) or LVL (e.g. MIV-1 and MIV-5) in the uppermost mantle but likely remains undetected if the data are not compared to those of undisturbed regions. The appearance of the $v_{s,\mathrm{app}}$ profile is clearly influenced by LVL or fast velocity layers which are at least a few tens of kilometres thick (e.g. MIV-20, MIV-50). We also find that a 50 km thick LVL with 10 per cent reduced mantle velocities and densities has an influence on the appearance of the $v_{s,\mathrm{app}}$ profile if its interface to an upper layer (either NM or NOC) is located at depths above ∼50 km b.s.f. (e.g. MI-50, MV-50). On the other hand, it should be noted that the search for a velocity model which explains a given $v_{s,\mathrm{app}}$ profile is non-unique (e.g. similarity of CIII and CM-REF) due to the trade-off between *S*-wave velocity and layer thickness. In the following section, we present the $v_{s,\mathrm{app}}$ profiles for real OBS data in the Eastern Mid Atlantic and describe a quantitative modelling approach to determine *S*-wave velocity-depth models which is designed based on the conclusion drawn in this section and the obtained $v_{s,\mathrm{app}}$ profiles of the real data.

5 APPLICATION TO REAL DATA

5.1 Data

Within the DOCTAR project (Deep OCean Test ARray), twelve broad-band OBSs were deployed in the Eastern Mid Atlantic (Fig. 8) approximately 60 km to 135 km North of the Gloria Fault which is part of the Eurasian–African plate boundary (Bird 2003).

The stations recorded seismometer and hydrophone data from July 2011 until April 2012. The array had an aperture of ∼75 km and was located in 4.5 km to 5.5 km water depth. One of the twelve stations had two clamped components (filled red triangle in Fig. 8, Hannemann *et al.* 2014), therefore we do not use the data from this station for our analysis. The data are time corrected (Hannemann *et al.* 2014) and the horizontal components are oriented by using *P* phases and Rayleigh phases (Stachnik *et al.* 2012; Sumy *et al.* 2015) of know teleseismic events.

For the analysis, we exclude all events for which a strong resonance with periods between 0.5 to 4 s (depending on the station, Figs 9a–c for station D03) is observed and for which this resonance has a clear influence on the estimated polarization angle (e.g. Fig. 9d). The observed resonance has a specific period range for each station which can also be identified in the probabilistic power spectral density (PPSD) of all three components by elevated amplitudes (Figs 9a–c at ∼3 s for station D03). We think that this resonance is related to the sedimentary cover in which wave energy is trapped. The resonance is triggered by ambient noise as well as body waves (compare Figs 9d and e before and after the *P*-wave arrival). Furthermore, an incoming *P*-wave at station D03 initially results in a resonance signal on the Z and the R component. Approximately 9 s later, an increasing resonance is observed on the T component (Fig. 9e). It is beyond the scope of this study to further describe or analyse this phenomenon. We only analyse events and period ranges for which the earthquake signal is visible in the recordings and stronger than the resonance signal. We also exclude all periods shorter than the corner period of the event recording from the analysis.

We use one to five events at the different stations and analyse in total 33 events at all stations (Tables 5 and 6 and Fig. 10). We choose the window length for the deconvolution for the (Z, R) RFs for each event based on the quality of the recorded signal. For the damping parameter of the Wiener filter, we use 0.01. Furthermore, we include all apparent *P*-wave incidence angle measurements in the analysis, for which the SNR on Z_{RF} and R_{RF} is larger than 4 (signal time window [−10 s, 10 s] and noise time window [−55 s, −25 s] relative to the direct *P* spike). We select the weight w_n in eq. (11) to be the SNR on R_{RF}.

It is likely that serpentinite is present in either the oceanic crust or mantle close to a major transform fault like the Gloria fault (White *et al.* 1992). Therefore, we do not put any constrains on v_p/v_s ratios by using the grid search presented in Section 4 rather than the root search to estimate the median $v_{s,\mathrm{app}}$ profiles shown in Fig. 10. We use the period range between 0.5 and 16.0 s for the analysis, because of the band limited nature of the earthquake signals and a known high self-noise level of the used instruments for periods longer than 10 s (Stähler *et al.* 2016, and Figs 9a–c). In order to show the variability of the results, we obtain the $v_{s,\mathrm{app}}$ profiles for each event (Tables 5 and 6) and each tested density ρ_1 (1.0–6.0 g cm^{-3} in 0.1 g cm^{-3} steps). We define a grid with cells centred at all used corner periods T_l and all possible apparent *S*-wave velocities $v_{s,\mathrm{app}}$ and count the crossings (hits) of all $v_{s,\mathrm{app}}$ profiles for each grid cell (grey-scale plots in Fig. 10). This visualization gives the opportunity to get an idea about the uncertainties of the obtained result. We observe that the real data estimates for $v_{s,\mathrm{app}}$ often show a multimodal distribution for each period T_l which represents the individual events. Therefore, the median profile of the total misfit and the weighted hit-count of the individual event's estimates are, in our opinion, a better representation of the result and its uncertainties than the mean and its standard deviation.

The *S*-wave velocities of NOC and NM are given by the dashed grey lines in Fig. 10. This shows that for the majority of the OBS (except D07 and D10, Figs 10f and i) the shorter periods

Downloaded from http://gji.oxfordjournals.org/ at GEOMAR Helmholtz-Zentrum fuer Ozeanforschung Kiel on November 23, 2016

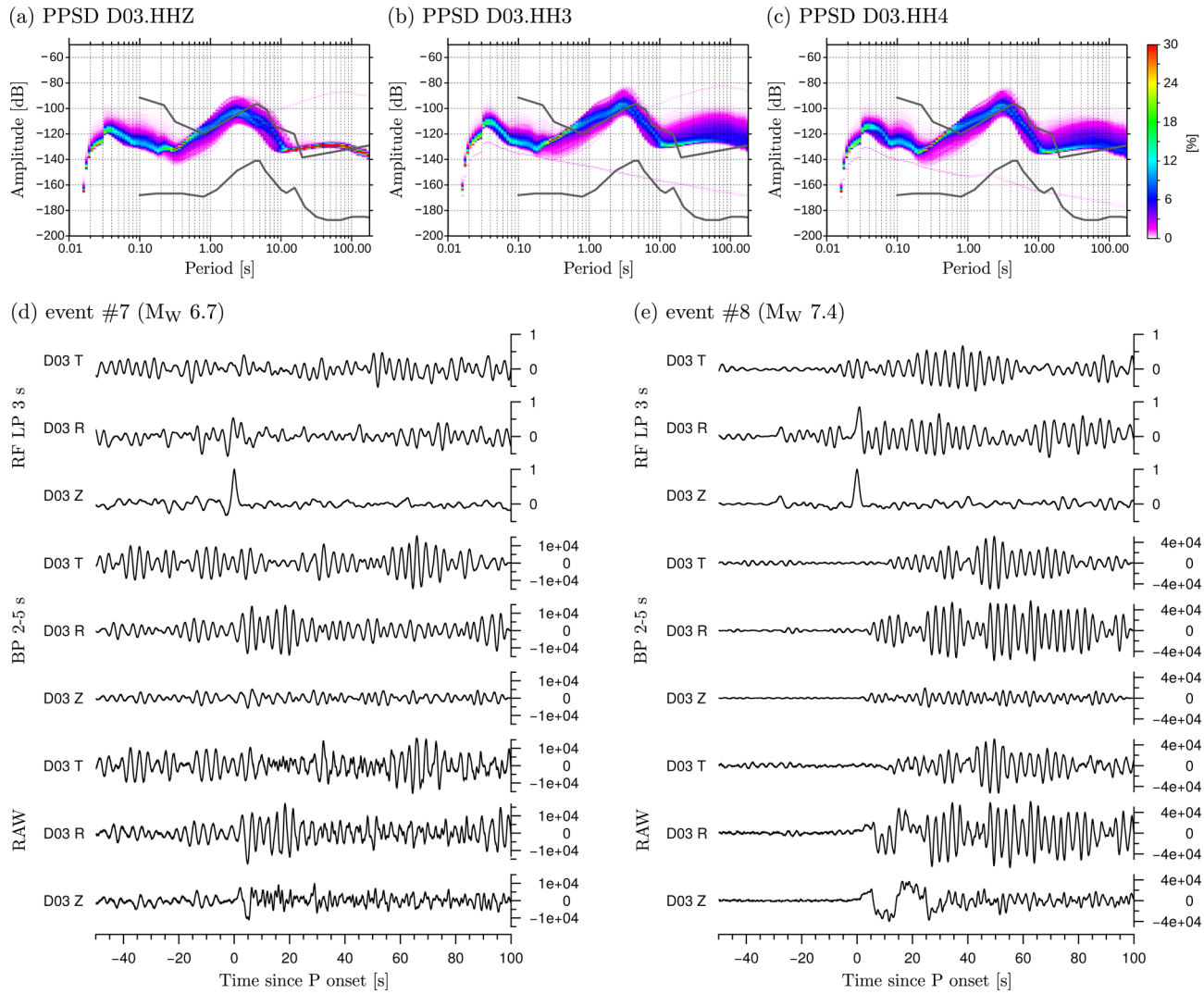

Figure 9. (a) Probabilistic power spectral density (PPSD; McNamara & Buland 2004) for vertical component (HHZ) of station D03 for recording period of 10 months. New High and Low Noise Model (Peterson 1993) is shown in grey. (b) Same as (a), but for not oriented horizontal component HH3. (c) Same as (a), but for not oriented horizontal component HH4. (d) Data example for event #7 at station D03 which has not been used in the following analysis. From bottom to top, the three traces for raw data (in counts), filtered data (in counts, bandpass 2 s to 5 s) and the low-pass filtered (3 s) receiver functions (normalized to P peak on Z) are shown. (e) Same as (d), but for event #8 which has been used in the following analysis.

Table 6. Events (Table 5) used at single stations for analysis of *P*-wave polarization and as presented in Fig. 10.

#	D01	D02	D03	D04	D06	D07	D08	D09	D10	D11	D12
1			X		X	X	X				
2					X						
3					X		X				
4		X	X	X			X	X	X	X	
5						X					
6									X		
7						X	X		X		
8	X		X	X	X	X	X			X	X
9		X		X	X						
10		X								X	
11			X								
Total	1	3	4	3	5	4	5	1	3	3	1

show smaller velocities than NOC. On the other hand, *S*-wave velocities similar or larger than NM are observed at longer periods (Fig. 10). Station D09 (Fig. 10h) has a data set which is limited to the period range 0.5–8 s. At station D07 (Fig. 10f), the longer periods (>4 s) might be biased by noise (compare Supporting Information Fig. S2). The $v_{s,\mathrm{app}}$ profiles of single events at station D11 (Fig. 10j) show *S*-wave velocities close to and larger than mantle *S*-wave velocities at longer periods (>4 s) which might be an indication for a different influence of noise on the single events. At stations D06, D08 and D10, the median $v_{s,\mathrm{app}}$ profile is dominated by different events (Figs 10e, g and i). This leads to a kink in the $v_{s,\mathrm{app}}$ profile at station D08 (∼4 s, Fig. 10g). At station D06, we observe a jump from $v_{s,\mathrm{app}}$ which are larger than mantle *S*-wave velocities to velocities similar to crustal *S*-wave velocities (∼4 s, Fig. 10e). A small jump from $v_{s,\mathrm{app}}$ which are larger than crustal *S*-wave velocities to crustal S wave velocities is visible at station D10 (∼0.7 s, Fig. 10i).

Overall, the $v_{s,\mathrm{app}}$ profiles can be divided into two groups: those which have a continuous appearance (D01-D04, D09, D10, D12,

Downloaded from http://gji.oxfordjournals.org/ at GEOMAR Helmholtz-Zentrum fuer Ozeanforschung Kiel on November 23, 2016

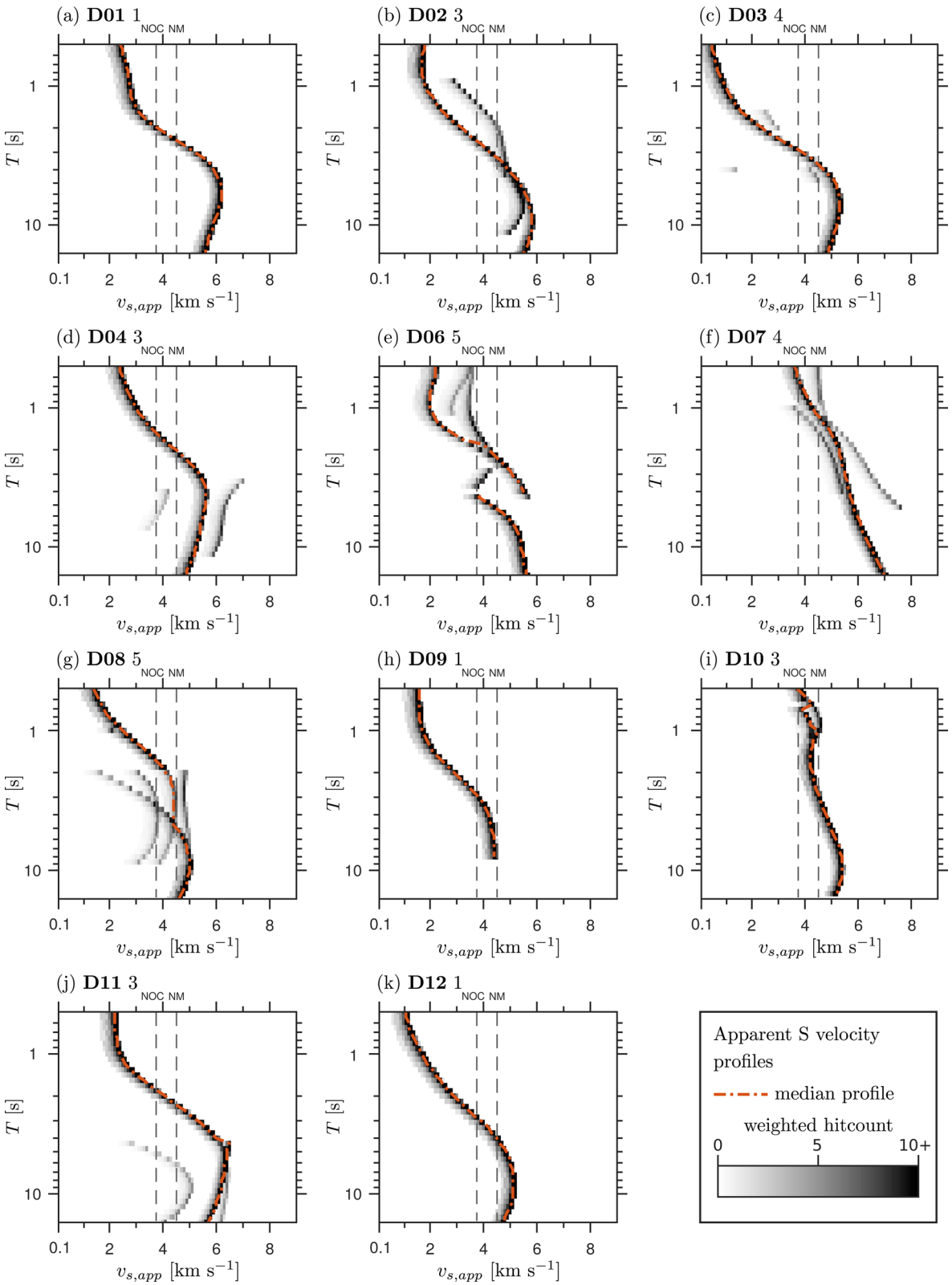

Figure 10. Weighted hit-counts of $v_{s,\mathrm{app}}$ profiles and median profiles of total misfit (eq. 11) for real data. We used the weights w_n which were applied to form the total misfit to estimate the weighted hit-counts. Station names are given in bold and number of events in normal font. The specific events are given in Tables 5 and 6. The *S*-wave velocities of normal oceanic crust (NOC) and normal mantle (NM) are marked with grey dashed lines.

Downloaded from http://gji.oxfordjournals.org/ at GEOMAR Helmholtz-Zentrum fuer Ozeanforschung Kiel on November 23, 2016

Figs 10a–d, h, i, k) and those which have jumps and kinks (D06, D08 and D11, Figs 10e, g and j) or are probably influenced by noise at longer periods (D07, Fig. 10f).

5.2 Quantitative modelling approach

In this section, we develop a quantitative modelling approach based on the observation made for the $v_{s,\mathrm{app}}$ profiles in the previous section (Fig. 10) and the conclusions drawn from the synthetic tests (Figs 4–7). In order to reduce the number of forward models needed, we use a unified water depth of 5.05 km as we saw that in the deep ocean the water depth has only a minor influence on the appearance of the $v_{s,\mathrm{app}}$ profiles (Fig. 6a). For the solid part of the model, we conclude from the $v_{s,\mathrm{app}}$ profiles of most of the OBS which have slower velocities than NOC at short periods that at least three solid layers above PREM b.s.f. are needed for the quantitative modelling. These layers represent sediment, crust and uppermost mantle, and we will search for the thickness of sediment (d_s) and crust (total crustal thickness $d = d_c + d_s$), as well as the *S*-wave velocities of all three layers (sediment, v_{ss}; crust, v_{sc}; uppermost mantle v_{sm}). The third solid layer (uppermost mantle) extends to a depth of 150 km b.s.f at which PREM takes over.

The calculation of the synthetic seismograms is performed by using the same source site model (PREM without ocean, Supporting Information Fig. S1) as for the synthetic teleseismic tests (Figs 6 and 7). A double couple with the same properties as for the synthetic tests in Figs 6 and 7 is chosen as source, but this time the source is seen from a back azimuth of 229° in an epicentral distance of 72.1° which corresponds to event #8 of the analysed real data (Table 5). We model the data by comparing the obtained median $v_{s,\mathrm{app}}$ profiles ($\tilde{v}^{\mathrm{obs}}_{s,\mathrm{app}}$) to the profiles which are determined from the synthetic seismograms ($\tilde{v}^{\mathrm{syn}}_{s,\mathrm{app}}$). Furthermore, we estimate whether the tested model ($\tilde{v}^{\mathrm{syn}}_{s,\mathrm{app}}$) performs better or worse than a predefined reference model ($\tilde{v}^{\mathrm{ref}}_{s,\mathrm{app}}$) in properly matching the real data results. For this purpose, we define an objective function R which is the ratio of the rms value of the weighted difference between $\tilde{v}^{\mathrm{obs}}_{s,\mathrm{app}}$ and $\tilde{v}^{\mathrm{syn}}_{s,\mathrm{app}}$ ($\mathrm{rms}_{\mathrm{obs-syn}}$) and the rms value of the weighted difference between $\tilde{v}^{\mathrm{obs}}_{s,\mathrm{app}}$ and $\tilde{v}^{\mathrm{ref}}_{s,\mathrm{app}}$ ($\mathrm{rms}_{\mathrm{obs-ref}}$).

$$R = \frac{\mathrm{rms}_{\mathrm{obs-syn}}}{\mathrm{rms}_{\mathrm{obs-ref}}} = \sqrt{\frac{\sum_{l=1}^{L}\left(\tilde{v}^{\mathrm{obs}}_{s,\mathrm{app}}(T_l) - \tilde{v}^{\mathrm{syn}}_{s,\mathrm{app}}(T_l)\right)^2 \cdot w_l}{\sum_{l=1}^{L}\left(\tilde{v}^{\mathrm{obs}}_{s,\mathrm{app}}(T_l) - \tilde{v}^{\mathrm{ref}}_{s,\mathrm{app}}(T_l)\right)^2 \cdot w_l}} \tag{13}$$

The objective function R is calculated for L different corner periods T_l. The weights $w_l = \tilde{w} \cdot w_p(T_l)$ are the medians $\tilde{w}$ of the $\mathrm{SNR_R}$ values (w_n in eq. 11) of the contributing measurements at period T_l times an optional, individual weight for different period ranges ($w_p(T_l)$, Fig. 11). The value for R is smaller than 1 if the median $v_{s,\mathrm{app}}$ profile of the current tested model matches $\tilde{v}^{\mathrm{obs}}_{s,\mathrm{app}}$ better than $\tilde{v}^{\mathrm{ref}}_{s,\mathrm{app}}$. On the other hand, R is larger than 1 if the current tested model performs worse than the reference model. We therefore search for the minimum in R to find the best performing model.

In order to limit the number of model parameters, we fix the v_p/v_s ratio a_x and the density ρ_x which we need for the modelling with QSEIS. The variable x refers to either sediment (s), crust (c) or mantle (m). The densities ρ_x are estimated by using the Nafe-Drake curve given by Brocher (2005) (eq. 12).

We choose a fine grid to sample our possible model space. We vary the *S*-wave velocity of the sediment (v_{ss}) between 0.1 and 2 km s^{-1}, the *S*-wave velocity of the crust (v_{sc}) between 2.5 and 4.5 km s^{-1} and the *S*-wave velocity of the uppermost mantle (v_{sm}) between 4.0 and 6.0 km s^{-1} in steps of 0.1 km s^{-1} (Fig. 11). The sediment thickness (d_s) is varied between 0.1 and 1 km in steps of 0.1 km and the total crustal thickness (d) between 4 and 12 km in 0.5 km steps (Figs 11a and b). This results in nearly 1.5 million models which need to be modelled and tested to sample the whole 5-D model space. To reduce the computational effort, we therefore use the depth sensitivity of the $v_{s,\mathrm{app}}$ profile for different period ranges by employing a three step quantitative modelling, although

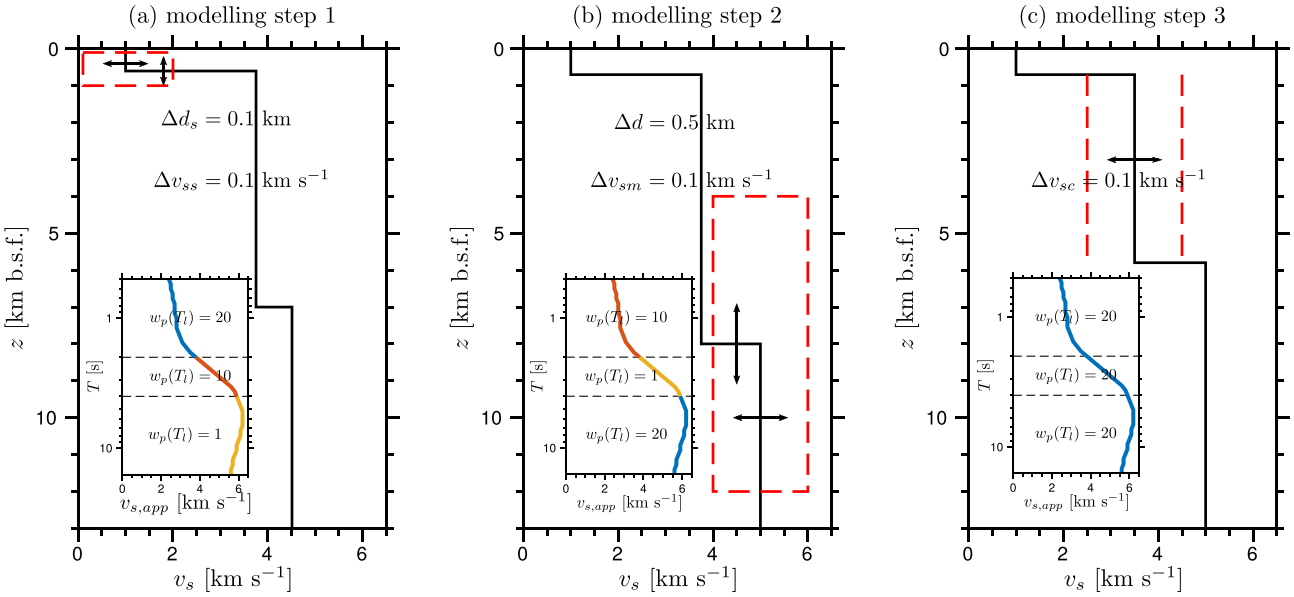

Figure 11. Illustration of the parameters and weighting used for the three step quantitative modelling approach. The parameter ranges are shown by red dashed boxes. The weighting of the different period ranges are given in the inset figure. (a) First modelling step: Search for the *S*-wave velocity v_{sc} and the thickness d_s of the sediment and the chosen weights $w_p(T_l)$ for this step. (b) Second modelling step: Search for the *S*-wave velocity of the mantle v_{sm} and the total thickness of the crust d and the weights $w_p(T_l)$ for this step. (c) Third modelling step: Search for the *S*-wave velocity of the crust v_{sc} and the equally chosen weights $w_p(T_l)$.

Downloaded from http://gji.oxfordjournals.org/ at GEOMAR Helmholtz-Zentrum fuer Ozeanforschung Kiel on November 23, 2016

this approach might not be suited to sample the whole 5D model space.

In the first step, we concentrate on the sedimentary layer and vary its *S*-wave velocity v_{ss} and its thickness d_s (0.1 km s^{-1} < v_{ss} < 2 km s^{-1} in 0.1 km s^{-1} steps, 0.1 km<d_s <1 km in 0.1 km steps, Fig. 11a). The *P*-wave velocity v_{ps} is determined by using an arbitrary v_p/v_s ratio a_s which is chosen in dependence on the *P*-wave velocities of the WC (v_{pw}, Table 1) and the NOC (v_{pc0}, Table 1):

$$a_s = \begin{cases} 4+n & \text{if } 4 \cdot v_{ss} < v_{pw} \text{ with } n \in \mathbb{N} \wedge n > \frac{v_{pw}}{v_{ss}} - 4 \\ 4 & \text{if } 4 \cdot v_{ss} > v_{pw} \wedge 4 \cdot v_{ss} < \frac{v_{pc0}}{2} \\ \sqrt{3} & \text{if } 4 \cdot v_{ss} > \frac{v_{pc0}}{2} \end{cases}, \quad (14)$$

in which the value n is a natural number. The density ρ_s is calculated using eq. (12). The crustal and the mantle layer have the properties of NOC and NM (Table 1) and the total crustal thickness d is set to 7 km. As reference model for estimating $\tilde{v}^{\text{ref}}_{s,\text{app}}$, we choose CM-REF (Table 3) which has a 5.05 km thick WC, no sediment layer, a 7 km thick NOC and an NM above PREM. We search for the minimum in the objective function $R(v_{ss}, d_s)$ (eq. 13). We learned from the results of the synthetic tests CI and CII (Fig. 7) that an LVL in the upper crust influences mainly the shorter periods of the $v_{s,\text{app}}$ profile, conclusively the weights $w_p(T_l)$ in eq. (13) for the individual period ranges are chosen to be higher for shorter periods than for longer periods (inset in Fig. 11a). The model resulting from the first step is used as reference model in the next modelling step.

After determining the sediment properties, a natural procedure would be to continue with the crustal velocity and thickness. Examining the $v_{s,\text{app}}$ profile of the model CI reveals that the period range in which the crustal properties influence the appearance of the profile is hard to isolate (Fig. 7a). On the other hand, the longer periods are clearly influenced by the mantle properties (Figs 7b and c). The second modelling step therefore focuses on the uppermost mantle *S*-wave velocity v_{sm} and the total crustal thickness d (4 km s^{-1} < v_{sm} < 6 km s^{-1} in 0.5 km s^{-1} steps, 4 km<d <12 km in 0.5 km steps, Fig. 11b). The properties of the sedimentary layer (v_{ss} and d_s) are kept constant at the values estimated in the first modelling step. We select higher weights $w_p(T_l)$ in eq. (13) for the longer period range. Moreover, we give higher weights $w_p(T_l)$ in eq. (13) to the shorter periods than the intermediate period range (inset in Fig. 11b), because the properties of the sedimentary layer have been determined in the first modelling step. The v_p/v_s ratio is $a_m = 1.8$ which is typical for oceanic mantle. Eq. (12) is used to estimate ρ_m. The velocities and the density of the crust are kept at the values for NOC (Table 1). Analogue to the first step, the minimum in the objective function $R(v_{sm}, d)$ (eq. 13) is searched and the corresponding model serves as reference model for the next step of the modelling.

In the third and last step, we search for the crustal *S*-wave velocity v_{sc} (2.5 km s^{-1} < v_{sc} < 4.5 km s^{-1} in 0.1 km s^{-1} steps, Fig. 11c). The values for the *S*-wave velocities of the sediment v_{ss} and the mantle v_{sm}, as well as the thickness of the sediment d_s and the total crustal thickness d are kept constant at the values resulting from the first two modelling steps. The weights $w_p(T_l)$ in eq. (13) are equal (inset in Fig. 11c). The *P*-wave velocity of the crust is estimated by using a standard v_p/v_s ratio of $a_c = \sqrt{3}$ and the density ρ_c is calculated by using eq. (12). Similarly to the other steps, the minimum in $R(v_{sc})$ (eq. 13) is searched and the resulting model is the best performing model for this quantitative modelling.

5.3 Results of quantitative modelling

The results of the single modelling steps described in Section 5.2 are shown for station D03 as an example (Fig. 12). In the first step, as described before, we search for the *S*-wave velocity of the sediment v_{sc} and its thickness d_s by looking for the minimum in the objective function $R(v_{ss}, d_s)$ (Fig. 12a). In case of station D03, this results in a model with $v_{ss} = 0.7$ km s^{-1} and $d_s = 0.6$ km (red cross in Fig. 12a) which serves then as reference model for the next modelling step.

In the second step, we vary the mantle *S*-wave velocity v_{sm} and the total crustal thickness d (Fig. 12b). For station D03, the value of $R(v_{sm}, d)$ is larger than one for all parameter combinations (Fig. 12b) meaning that the reference model ($\tilde{v}^{\text{ref}}_{s,\text{app}}$) always performs better than each tested model ($\tilde{v}^{\text{syn}}_{s,\text{app}}$). We therefore keep the model with $v_{ss} = 0.7$ km s^{-1}, $d_s = 0.6$ km, $v_{sm} = 4.51$ km s^{-1} and $d = 7$ km as reference model for the last step of the modelling.

In the third step, we look for the crustal *S*-wave velocity v_{sc} by searching the minimum in $R(v_{sc})$ (Fig. 12c). The result, which is found for $R(v_{sc})$ slightly below 1, gives the best performing model for station D03 ($v_{ss} = 0.7$ km s^{-1}, $d_s = 0.6$ km, $v_{sm} = 4.51$ km s^{-1}, $d = 7$ km and $v_{sc} = 4.3$ km s^{-1}, Fig. 12c).

Instead of concentrating just on the minimum value of the objective function R (R_{min}), we give an arbitrary range of R which includes all models for which $R <= R_{\text{min}} + 0.1$ (black lines in Figs 12a–c) is valid in order to get an idea of the stability of the gained results and the sharpness of the obtained minimum in R. Moreover, we choose additional reference models to repeat step two and three of the modelling. These models represent alternative allowed parameter combinations in $R(v_{ss}, d_s)$ (e.g. yellow circles in Fig. 12a) or $R(v_{sm}, d)$ (e.g. black cross in Fig. 12b). In the latter case, they are sometimes chosen outside the $R_{\text{min}} + 0.1$ range if $R(v_{sm}, d)$ shows several areas with small values close to $R_{\text{min}} + 0.1$. Furthermore, if the models with small $R(v_{sm}, d)$ values have high mantle *S*-wave velocities (>5.5 km s^{-1}) or a large total crustal thickness (>10 km), we perform an additional test in the third modelling step with a model which has NM properties and a total crustal thickness of 7 km and the sedimentary properties resulting from step one.

In order to get an idea about the variability of the obtained models and to present all models at once, we compare all $v^{\text{syn}}_{s,\text{app}}$ profiles of all models which met the criteria $R <= R_{\text{min}} + 0.1$ for each step of the quantitative modelling to the real data $v^{\text{obs}}_{s,\text{app}}$ profile with equal weights in all period ranges. For this comparison, the objective function R (eq. 13) is calculated by using the model CM-REF (5.05 km WC, 7 km NOC and NM above PREM) as reference model. The resulting value of R is used to calculate a weighting factor $(1 - R)$ for a weighted hit-count of the used velocity models. For the visualization (Fig. 12d), we additionally weight the different layers according to the different period ranges (insets in Fig. 11), for example, for a model, which results from the first step of the quantitative modelling, the sediment layer is weighted with 20 as for the period range from 0.5 to 2 s, the crust with 10 as for the period range from 2 to 4 s and the mantle with 1 as for the period range from 4 to 16 s. The models resulting from the other steps are treated in a similar way. This procedure is applied to reduce the biasing effect of models with NM and NOC properties in the first two steps on the hit count. The red dash-dot line in Fig. 12(d) shows the model with $v_{ss} = 0.7$ km s^{-1}, $d_s = 0.6$ km, $v_{sm} = 4.51$ km s^{-1}, $d = 7$ km and $v_{sc} = 4.3$ km s^{-1} (Table 7) which has the smallest value of $R(v_{sc})$ in Fig. 12(c). Furthermore, we utilize the weighting factor $(1 - R)$ to estimate the weighted hit-count of the $v_{s,\text{app}}$ profiles (Fig. 12e).

Downloaded from http://gji.oxfordjournals.org/ at GEOMAR Helmholtz-Zentrum fuer Ozeanforschung Kiel on November 23, 2016

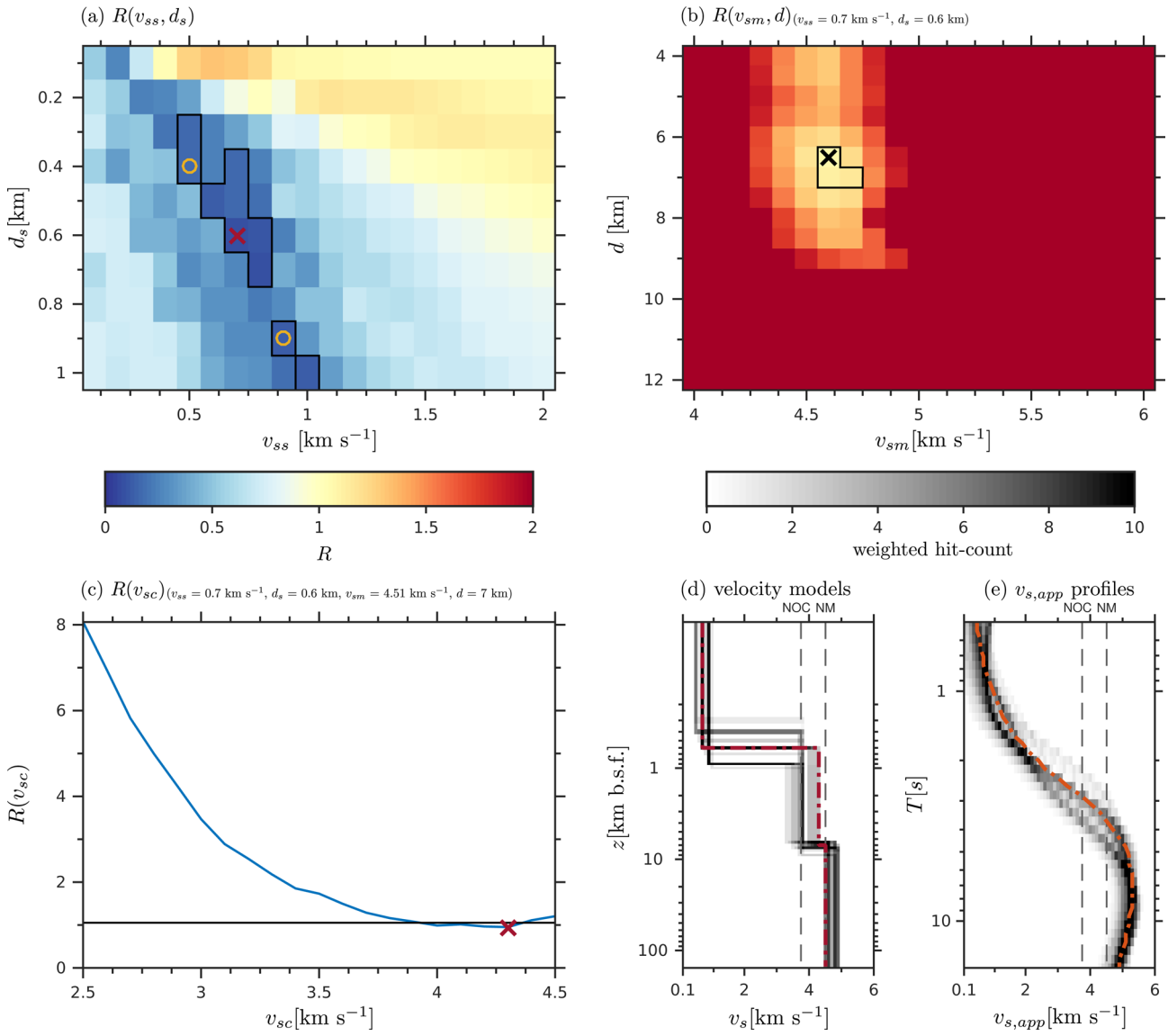

Figure 12. Example for modelling steps for station D03: (a) Ratio R (eq. 13) shown in dependence on sediment S-wave velocity v_{ss} and thickness d_s. The reference model is CM-REF (Table 3). The model with the smallest value of R (R_{min}) is marked with a red cross. Additional models tested in step 2 are marked with yellow circles. The area with $R <= R_{\text{min}} + 0.1$ is outlined with black. (b) Ratio R is shown in dependence on mantle S-wave velocity v_{sm} and total crustal thickness d, the best fitting model of step one is chosen as reference model (red cross in panel a, $v_{ss} = 0.7$ km s^{-1} and $d_s = 0.6$ km). The cross marks R_{min} and the area with $R <= R_{\text{min}} + 0.1$ has a black contour. (c) Ratio R is shown in dependence on crustal S-wave velocity v_{sc}, the best fitting model of step one is chosen as reference model (red cross in panel a, $v_{ss} = 0.7$ km s^{-1}, $d_s = 0.6$ km, $v_{sm} = 4.51$ km s^{-1} and $d = 7$ km). The red cross marks R_{min} and $R = R_{\text{min}} + 0.1$ is indicated by a black line. (d) Weighted hit-count of the velocity models resulting from all chosen reference models for all three steps (38 in total, 36 for all reference models with $R < R_{\text{min}} + 0.1$). The best performing model with smallest value $R(v_{sc})$ in (c) is shown as red dash-dot line ($v_{ss} = 0.7$ km s^{-1}, $d_s = 0.6$ km, $v_{sm} = 4.51$ km s^{-1}, $d = 7$ km and $v_{sc} = 4.3$ km s^{-1}). (e) Weighted hit-count of corresponding $v_{s,\text{app}}$ profiles for all models in (d) in comparison to real data (orange dash-dot line). The S-wave velocities of normal oceanic crust (NOC) and normal mantle (NM) are given as grey dashed lines in (d) and (e).

It is clear by comparing Figs 12(a) and (b) that if more models are lying within the $R < R_{\text{min}} + 0.1$ area, the minimum in the ratio R is less sharp. If a smaller number of models fulfils this requirement, the resulting velocity models can be regarded as better constrained by the available data. The total number of models estimated for station D03 is 38. This number includes 36 models which result from choosing reference models in step one and two within the $R < R_{\text{min}} + 0.1$ range and 2 models which result from an additional reference model chosen in step two from a separate area in R with small R values close to the $R < R_{\text{min}} + 0.1$ range.

We repeat all three steps of the modelling for each station (Fig. 10) and present the obtained results (velocity models and their corresponding $v_{s,\text{app}}$ profiles, as well as number of models) in Fig. 13 and the parameters of the best performing models in Table 7.

6 DISCUSSION

6.1 Discussion of quantitative modelling results

The best performing models at most stations show three distinct solid layers (Figs 12d and 13). The stations D03 and D09 are exceptions to this overall trend. At these stations the crustal and the mantle S-wave velocities are quite similar (Figs 12d and 13g). For

Downloaded from http://gji.oxfordjournals.org/ at GEOMAR Helmholtz-Zentrum fuer Ozeanforschung Kiel on November 23, 2016

Table 7. Model parameters for best performing models for each station as presented in Figs 12 and 13: *S*-wave velocity of sediment v_{ss}, mantle v_{sm} and crust v_{sc}, and sediment thickness d_s and total crustal thickness d. Poorly resolved model parameters are indicated by an asterisk.

Station	v_{ss}	d_s	v_{sm}	d	v_{sc}
D01	1.2	0.8	5.3	4.5	3.5
D02	1.0	0.7	5.2	7.0	3.75
D03	0.7	0.6	4.51	7.0	4.3
D04	1.2	0.8	4.8	5.0	4.1
D06	0.9	0.4	5.3	10.0*	3.8
D07	1.4	0.3	5.9*	5.5	4.1
D08	0.8	0.3	4.7	9.0*	3.6
D09	1.0	0.7	4.0*	7.0	3.9
D10	1.4*	0.3*	5.0	6.5	3.75
D11	1.2	0.9	5.5*	4.0	3.7
D12	0.9	0.8	4.6	5.5	3.75

station D03, we have a crustal *S*-wave velocity of 4.3 km s^{-1} which is closer to typical mantle *S*-wave velocities. The weighted hit-count plot for all models within the $R < R_{\min} + 0.1$ range (Fig. 12d) shows that the crustal *S*-wave velocity varies between 3.5 and 4.3 km s^{-1} and the mantle *S*-wave velocity lies in the range of 4.5–4.9 km s^{-1}. The velocities of the best performing velocity model therefore represent the fastest crustal and the slowest mantle *S*-wave velocities at station D03. On the other hand, we get a mantle *S*-wave velocity of 4.0 km s^{-1} for station D09 which is closer to a typical oceanic crustal velocity (Fig. 13g). This can be explained by the fact that for station D09, our result only relies on a $v_{s,\mathrm{app}}$ profile obtained from a single event in the period range between 0.5 and 8 s. It therefore is possible that the data set at station D09 is insufficient to constrain the uppermost mantle *S*-wave velocity at this station and just the sedimentary and crustal *S*-wave velocity are properly estimated.

At the stations D07 and D11, we probably observe the influence of noise on the longer periods (>4 s) of the median $v_{s,\mathrm{app}}$ profiles which leads to either higher $v_{s,\mathrm{app}}$ estimates (D07, Fig. 10f) or different velocity estimates for individual events (D11, Fig. 10j). In both cases, the influence of noise on the longer periods (>4 s) probably causes that the uppermost mantle *S*-wave velocities estimated by the quantitative modelling are rather high (Figs 13e and i).

The median $v_{s,\mathrm{app}}$ profiles at stations D06 and D08 show kinks and jumps at ∼4 s. The discontinuity in the profiles probably leads to biased estimates of the total crustal thickness. This becomes evident considering that at both station, models with large crustal thicknesses (9–10 km, Figs 13d and f) are favoured by the quantitative modelling.

Station D10 also shows a jump in its median $v_{s,\mathrm{app}}$ profile at 0.7 s (Fig. 10i) which is rather small compared to station D06. An influence on the estimated sedimentary model parameters might be possible. The overall appearance of the short periods (<2 s) of the $v_{s,\mathrm{app}}$ profiles at station D10 and D07 are similar and also the obtained sedimentary model parameters are in good agreement (Figs 13e and h), which indicates only a minor influence of the discontinuous $v_{s,\mathrm{app}}$ profile at station D10 on the obtained sedimentary models.

At station D04, the comparison of the median $v_{s,\mathrm{app}}$ profile and the modelled profiles shows slightly higher velocities in the period range between 2 and 4 s for the real data (Fig. 13c). These elevated velocities are probably related to the effect of the before mentioned resonance. Nevertheless, the good resemblance of the asymptotic behaviour of the median $v_{s,\mathrm{app}}$ profile at the short and long periods by the modelled profiles (Fig. 13c) assures us that the obtained models are reliable.

In order to consider all discussed effects at the single stations, poorly resolved model parameters are indicated by either superimposed grey shadings in Fig. 14 or lighter colours in Fig. 15.

In Fig. 14, we present an N–S and a W–E profile in which the best performing models are shown as columns. The sediment layers can be divided into two groups. The first group has a thickness between 0.3 km and 0.4 km (D06, D07, D08, D10) and the second between 0.6 km and 0.9 km (Fig. 14 and Table 7). The *S*-wave velocities in the sediments vary between 0.7 and 1.4 km s^{-1} (second layer in Fig. 14). We observe no clear correlation between water depth or location and sediment thickness or *S*-wave velocity. The different sediment thicknesses and varying *S*-wave velocities might be related to a rough basement topography with sediment filled depressions as can be seen on analogue seismic recordings of the area under investigation which were recorded in 1969 (NOAA World Data Service for Geophysics, Marine Seismic Reflection, Survey ID V2707, ngdc.noaa.gov). Moreover, we can relate the resonance observed at the OBS to the properties of the sedimentary layer. If we take the sediment thickness $d_s = 0.6$ km and the sediment *S*-wave velocity $v_{ss} = 0.7$ km s^{-1} at station D03 and a relation for the resonance frequency of sediments $f_r = v_{ss}/(4 \cdot d_s)$ (Parolai *et al.* 2002), we get a resonance period of 3.4 s which is similar to the observed period of the resonance at station D03 (∼3 s, Fig. 9). The periods obtained for the other stations also agree quite well with the observed periods of the resonance at each station.

The uppermost mantle *S*-wave velocities v_{sm} clearly decrease towards the South (lower layer in Figs 14 and 15a). In Fig. 15(a), we present all estimated v_{sm} which fulfil the criteria $R < R_{\min} + 0.1$ in the second step of the quantitative modelling. Assuming a linear trend gives a decrease of ∼23 m s^{-1} per km along the N–S profile. We interpret this decrease in uppermost mantle *S*-wave velocity as the influence of the Gloria Fault which lies South of the OBS array (Fig. 8). This decrease might be related to either biasing effects of anisotropy or out of plane arrivals, or changes in rheology, hydration or melt fraction. The azimuthal coverage of our data is too limited to allow any conclusions whether the observed decrease in *S*-wave velocity towards the fault is caused by anisotropy which might be present close to a major plate boundary like the Gloria fault (e.g. San Andreas fault, Ozacar & Zandt 2009). Furthermore, we exclude any influence by out of plane arrivals due to the small deviations (<3°) in back azimuth of the analysed events from theoretical values identified using a frequency-wave number analysis (Rost & Thomas 2002) on the vertical components of the OBS, and the similar results of the orientations using *P*-wave polarization and Rayleigh wave characteristics (Stachnik *et al.* 2012). On the other hand, a reduction in the *S*-velocity can also be caused by partial melt, different water contents, serpentinization or a change in grain sizes (Horen *et al.* 1996; Jung 2001; Faul & Jackson 2005; Stixrude & Lithgow-Bertelloni 2005; Karato 2012). Karato (2012) suggests that the amount of partial melt generated away from mid-ocean ridges is small and that the seismic velocity reduction due to small amounts of melt (<0.1 per cent) is small if grain boundaries are not completely wetted by the melt. In the vicinity of the Gloria Fault, fractures can be generated which can serve as pathways for the seawater to penetrate the oceanic lithosphere. This can change the fabric of the mantle minerals (Jung 2001) or leads to serpentinization (Fryer 2002). Both processes result in lower seismic velocities (Horen *et al.* 1996; Jung 2001). Fryer (2002) (and references therein) also gives an example in which the degree of serpentinization increases towards a shear zone, in-line with our

Downloaded from http://gji.oxfordjournals.org/ at GEOMAR Helmholtz-Zentrum fuer Ozeanforschung Kiel on November 23, 2016

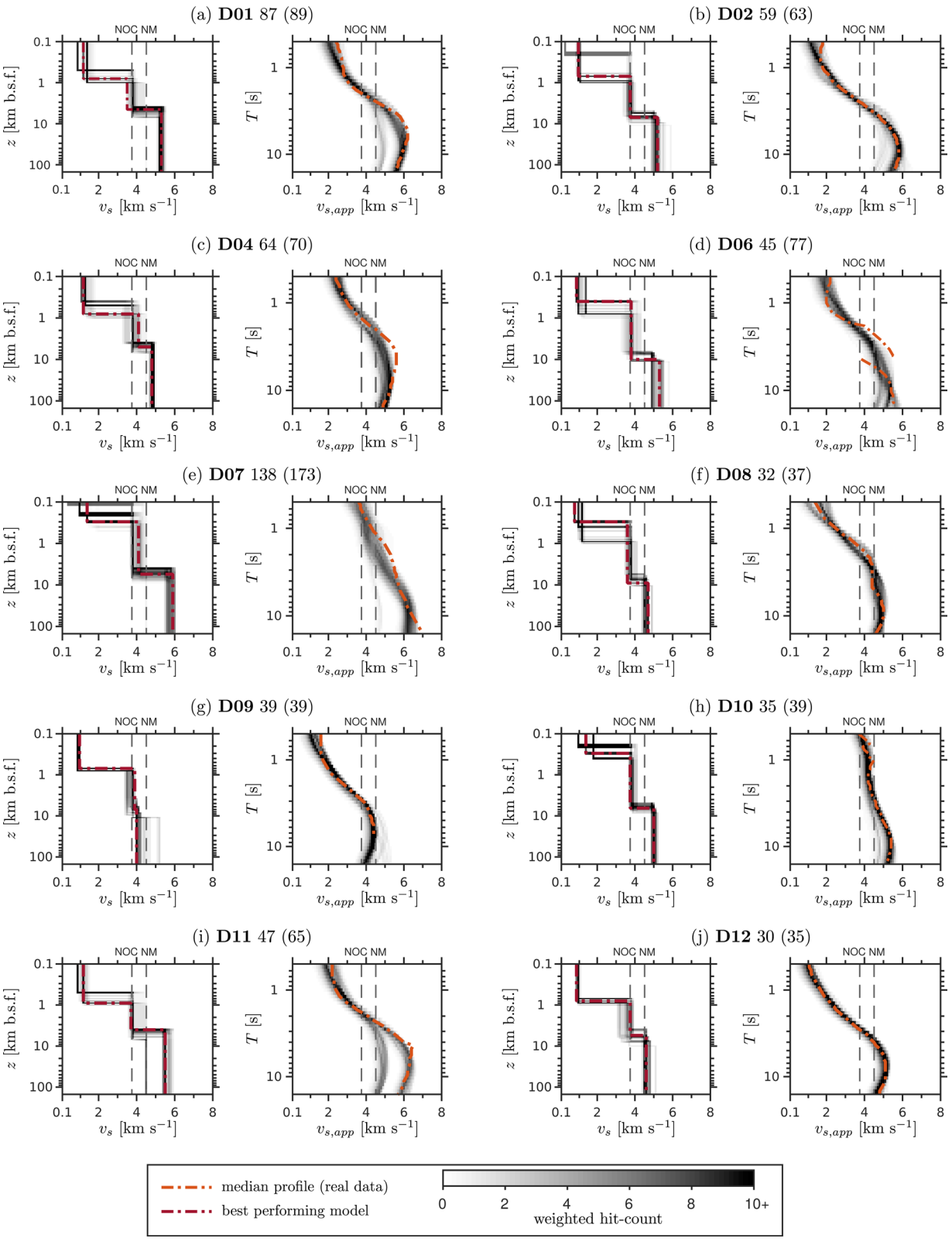

Figure 13. Weighted hit-count for velocity models and their corresponding $v_{s,\mathrm{app}}$ profiles for all stations besides D03. Same as Figs 12(d) and (e). Station names are given in bold. The number of models for which $R < R_{\mathrm{min}} + 0.1$ is valid is given for each station: those with reference models which fulfil $R < R_{\mathrm{min}} + 0.1$ in the previous modelling step and in brackets those for all used reference models.

Downloaded from http://gji.oxfordjournals.org/ at GEOMAR Helmholtz-Zentrum fuer Ozeanforschung Kiel on November 23, 2016

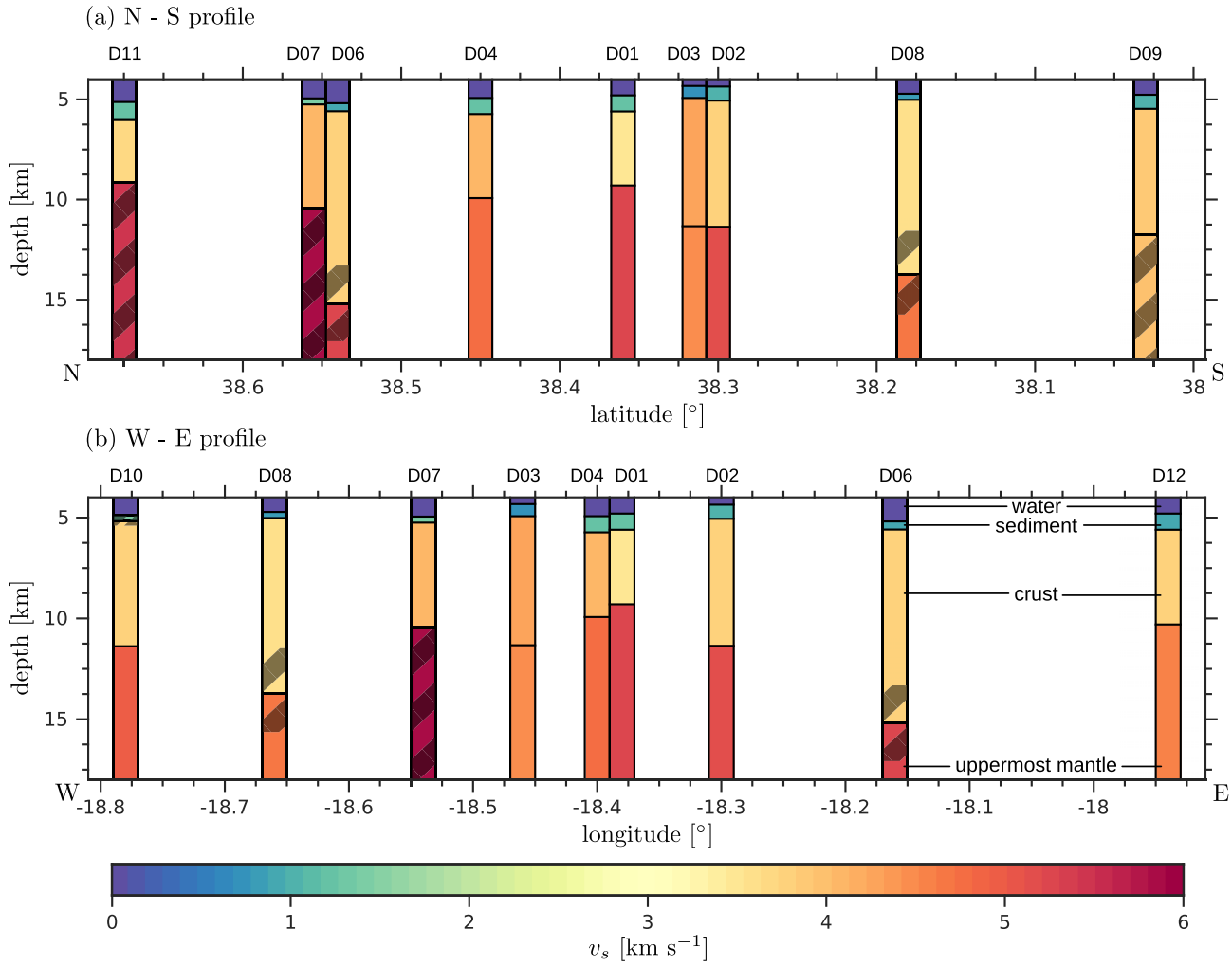

Figure 14. *S*-wave velocity depth profiles in (a) N–S and (b) W–E directions for best performing models as presented in Figs 12(e) and 13. Models are labelled with station names and water depth are taken from the ship echo-sounder. Poorly resolved model parameters mainly influenced by noise are superimposed with grey overlays.

observation of decreasing velocities towards the plate boundary (Horen *et al.* 1996). Another common feature of shear zones is the reduction of grain size in high shear strain areas by the formation of mylonites (Bürgmann & Dresen 2008). The grain size reduction causes a decrease in the shear modulus which is directly related to a decrease in seismic velocities (Faul & Jackson 2005). This effect may be a direct indication of an increase in shear strain in the direction of the plate boundary (Bürgmann & Dresen 2008). In conclusion, the observed velocity decrease towards the Gloria Fault probably results from the combined effects of serpentinization, an increase in water content and grain size reduction towards the fault. The serpentinization is probably the strongest of all effects discussed here, because of the abundance of serpentinite close to fractures in the oceanic crust and mantle (White *et al.* 1992).

The crustal *S*-wave velocities v_{sc} (third layer in Fig. 14) are quite similar across the array (3.5–4.3 km s^{-1}). The total crustal thickness d varies for most stations between 4 and 7 km and shows larger values at station D08 (9 km) and D06 (10 km). The thickness d shows no clear trend from the western to the eastern end of the array (Fig. 14). This behaviour is reasonable given that the difference in the crustal ages between the western station D10 (∼76.4 Ma, Müller *et al.* 2008) and the eastern station D12 (∼82.9 Ma, Müller *et al.* 2008) are quite small. In contrast, we observe a possible slight increase in the total crustal thickness towards the South, that is, towards the Gloria Fault (grey dashed line in Fig. 15b and Fig. 8) although the differences in crustal age are similar to the W-E direction. In Fig. 15(b), all total crustal thicknesses d, which fulfil the criteria $R < R_{\min} + 0.1$ in step two of the quantitative modelling, are shown as a function of distance along the N-S profile. The weak trend is still visible, although station D06 shows larger thicknesses than would be expected by the weak trend and station D09 has a large scatter in the estimated thickness. In the bathymetry (Fig. 8), nearly NE-SW striking bathymetric heights are visible which are an evidence for the known transpression in this region (Zitellini *et al.* 2009, fig. 6). This mechanism leads to a shortening in the crust which is larger in the vicinity of the fault. We interpret the gradual thickening of the estimated crustal thickness from N to S with the gradual shortening of the crust towards the Gloria fault.

6.2 Discussion of method

The proposed method relies on the proper estimation of the apparent *P*-wave incidence angle using RF which implies that data quality is essential especially in case of OBS at which only few event recordings are available (Webb 1998). In order to exclude recordings or period ranges which are highly influenced by noise or resonance

Downloaded from http://gji.oxfordjournals.org/ at GEOMAR Helmholtz-Zentrum fuer Ozeanforschung Kiel on November 23, 2016

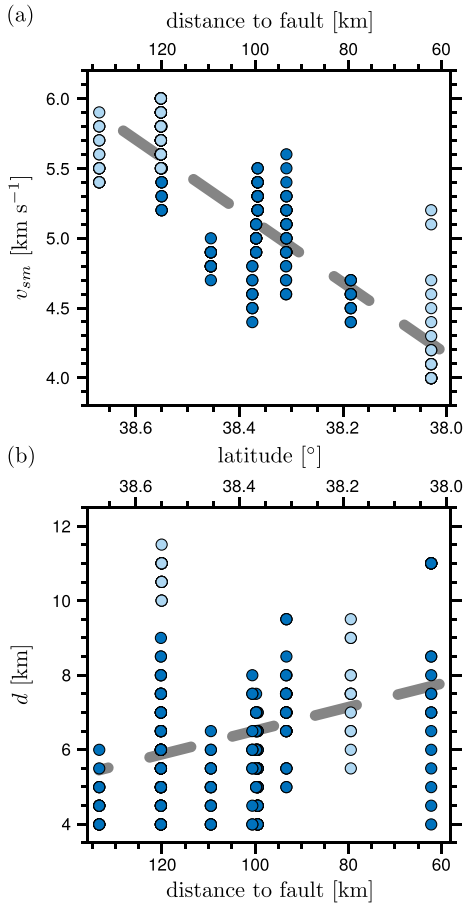

Figure 15. Estimated model parameters of second modelling step along N–S profile (Figs 11b and 14a) and against distance towards Gloria fault. All models fulfil $R < R_{\min}$ in the second quantitative modelling step. Analysing the parameters by assuming a linear trend gives the grey dashed lines. Poorly resolved model parameters are shown in lighter colours. (a) Uppermost mantle *S*-wave velocity v_{sm}. (b) Total crustal thickness *d*.

effects (e.g. Fig. 9), a careful data review is necessary. Some $v_{s,\mathrm{app}}$ profiles might be still influenced by noise especially at long periods (e.g. D07, >4 s, Fig. 10f and Supporting Information Fig. S2) or by resonance effects at intermediate periods (D04, Fig. 10d). This needs to be considered during the interpretation of modelling results. Moreover, we notice that the behaviour of the $v_{s,\mathrm{app}}$ at longer periods might be influenced by long period global phases (e.g. W phase, Kanamori 1993) or whether the deconvolution filter is correctly determined at these periods which is influenced by the Wiener filter parameters (Supporting Information Fig. S3). To ensure that apparent *P*-wave incidence angle measurement with a sufficient data quality are considered, we employ the SNR of the RF as criteria to select the data (SNR>4 at Z_{RF} and R_{RF}) and as weighting in eqs (11) and (13).

We also have to consider the corner period of the event's source spectrum and exclude all periods shorter than the event's corner period from the analysis. Additionally, the effect of the employed filter on the *P* spike might have an influence on the appearance of the $v_{s,\mathrm{app}}$ profile. Both, the *P* spike of a RF and the impulse response of a forward and backward applied low pass filter can be regarded as having a similar bell shape like a Gaussian function. Keeping this in mind, the convolution of a *P* spike with a corner period T_{cp} and an impulse response of a zero phase low pass filter with a corner period T_{cf} would result in a signal with an actual corner period $T_{ca}^2 = T_{cp}^2 + T_{cf}^2$. This effect is important for actual corner periods T_{ca} smaller than 2–3 times T_{cp}. We tested the correction of the corner periods for our first quantitative modelling step and found similar results as presented in Section 5. We conclude from this that the corner periods of the real and the synthetic data are similar enough that the effect of the filtering can be considered to be the same and therefore has not to be corrected.

In our case, all used Z_{RF} have an approximate bell shape. If an observed Z_{RF} would oscillate and deviate from a simple bell shape, the quantitative modelling presented here can still be applied by convolving the modelled RF with the observed Z_{RF} (Schiffer *et al.* 2015) before applying the low pass filters and comparing the $v_{s,\mathrm{app}}$ profiles.

We use an arbitrary v_p/v_s ratio for all three steps in the quantitative modelling of the OBS data (eq. 14 for the sediments, $v_p/v_s = \sqrt{3}$ for the crust and $v_p/v_s = 1.8$ for the mantle) to estimate the *P*-wave velocity v_p and the density ρ. If we replace our v_p/v_s ratio for the sediments (eq. 14) with the mud-rock line ($v_p = 1.16 \cdot v_s + 1.36$, Castagna *et al.* 1985), the obtained results for the first step of the quantitative modelling are similar to the results presented here. This underlines that the apparent *P*-wave incidence angle $\overline{\varphi}_p$ is independent of the *P*-wave velocity v_p of the ocean bottom which was already indicated by our relation in eq. (10), and the weak dependence of $\overline{\varphi}_p$ on the density ρ of the ocean bottom as already shown in Section 4.

7 CONCLUSION AND OUTLOOK

We derive the relations for the apparent *P*-wave incidence angle at the ocean bottom in dependence on the elastic parameters, the different reflection and refraction angles (eq. 9) and the slowness (eq. 10), respectively. The second relation reveals that the apparent *P*-wave incidence angle is independent of the *P*-wave velocity of the ocean bottom and theoretically depends on the apparent half-space *S*-wave velocity and the density of the ocean bottom. We show by employing synthetic half-space velocity models that the dependence on the *S*-wave velocity is much stronger than on the density (Fig. 3). Moreover, we observe a clear dependence of the obtained apparent *S*-wave velocities on the corner periods of the used low pass filters (Fig. 4). This confirms the hypothesis of Phinney (1964) that obtained seismic velocities from the analysis of the *P*-wave polarization depend on the used period range. Furthermore, it is in good agreement with the observations made for land stations by Svenningsen & Jacobsen (2007) and Kieling *et al.* (2011). The investigation of the influence of different parameters of a layered subsurface model on the appearance of the $v_{s,\mathrm{app}}$ profiles leads to the conclusion that a velocity increase and decrease can be identified and that the observed 'overshoot' in the $v_{s,\mathrm{app}}$ profiles is influenced by the layer thickness. Moreover, the $v_{s,\mathrm{app}}$ profiles show the tendency that the shorter periods converge towards the velocity of the uppermost layers and the longer periods toward the velocity of deeper layers. Besides a small influence of the water depth on the appearance of the $v_{s,\mathrm{app}}$ profiles, we find that the removal of water multiples might be useful for water depth shallower than ~1 km (Fig. 6; Osen *et al.* 1999; Thorwart & Dahm 2005) in order to prevent a distortion of the obtained results. We find from our synthetic test that the uppermost mantle shear wave velocity can be identified. However, LVLs deeper than 50 km are hardly resolvable (Fig 7).

We analyse OBS data which were recorded in the Eastern Mid Atlantic ~60 to 135 km North of the Gloria fault. We use a grid search for *S*-wave velocities in a layered Earth model for the

Downloaded from http://gji.oxfordjournals.org/ at GEOMAR Helmholtz-Zentrum fuer Ozeanforschung Kiel on November 23, 2016

quantitative modelling of the real ocean bottom data. Additionally, we identify a resonance signal with dominant periods between 0.5 and 4 s as a main reason for amplitude distortions and therefore erroneous apparent *P*-wave incidence angles. Events showing a clear influence of this resonance phenomenon on the obtained angles are removed from the analysis.

Overall, we find that models consisting of three solid layers (sediment, crust and uppermost mantle) over PREM b.s.f. are well suited to model the real data. The sediments can be grouped in two thickness ranges (0.3–0.4 km and 0.6–0.9 km), there is no water depth dependency which is in good agreement to known seismic profiles of the area. Furthermore, we find that the uppermost mantle shear wave velocity decreases towards the Gloria Fault. Additionally, we observe a crustal thickening towards the fault which agrees well with the known transpressive character of the plate boundary (Zitellini *et al.* 2009). We suggest that the decrease in uppermost mantle shear velocity and the crustal thickening towards the fault is deformation related.

The presented method of *S*-wave velocity estimation using *P*-wave polarization can be combined with surface wave methods and/or RFs in a joint inversion (e.g. Du & Fougler 1999; Julià *et al.* 2000; Schiffer *et al.* 2015) in order to better constrain the estimated model parameters. The obtained *S*-wave velocities can also be useful for further analysis of the experimental area. RFs can be used to estimate Moho depth and the *vp*/*vs* ratio of the crust by employing an amplitude stack of the direct crustal phase and its multiples (Zhu & Kanamori 2000). Usually, the needed delay times of the direct phase and the multiples are calculated by giving a *P*-wave velocity for the crust. An alternative approach might be that the obtained *S*-wave velocities of the apparent *P*-wave incidence angle analysis are used instead of an arbitrary *P*-wave velocity.

In conclusion, the proposed method is usable for single station estimates of the local *S*-wave velocity structure beneath the ocean bottom. The implementation of the method is easy and the processing is performed in two steps:

(1) measurement of apparent *P*-wave incidence angles in different period ranges for real and synthetic data;
(2) comparison of determined apparent *S*-wave velocity profiles for real and synthetic data.

The second step leads to the estimation of *S*-wave velocity-depth models.

ACKNOWLEDGEMENTS

KH thanks the Niedersächsische Staats- und Universitätsbibliothek in Göttingen for providing the digital copy of Wiechert (1907) and Zoeppritz (1919), as well as the Thüringer Universitäts- und Landesbiblitothek for providing the digital copy of Knott (1899). KH thanks Uwe Altenberger for discussing probable reasons for the change in the uppermost mantle velocities. The authors thank EMEPC (Task Group for the Extension of the Continental Shelf) for providing the bathymetric data and Luis Batista for sharing them. The authors are grateful to Bo Holm Jacobsen and an anonymous reviewer for their comments which helped to improve the manuscript. The data processing was partly done using Seismic Handler (Stammler 1993). The power spectral densities were obtained with obsPy (Beyreuther *et al.* 2010). Some figures were created using GMT (Generic Mapping Tools, Wessel *et al.* 2013). The authors thank the DEPAS (Deutscher Gerätepool für amphibische Seismologie/German instrument pool for amphibian seismology) pool for providing the instruments for the DOCTAR project which was funded by the DFG (Deutsche Forschungsgemeinschaft/German Research Foundation) (KR1935/13, DA 478/21-1) and by the Leitstelle für Mittelgroße Forschungsschiffe (Poseidon cruises 416 and 431).

REFERENCES

Aki, K. & Richards, P.G., 2002. *Quantitative Seismology,* 2nd edn, University Science Books.
Ammon, C., 1991. The isolation of receiver effects from teleseismic P waveforms, *Bull. seism. Soc. Am.,* **81**(6), 2504–2510.
Ben-Menahem, A. & Singh, S.J., 1981. *Seismic Waves and Sources,* Springer Verlag.
Beyreuther, M., Barsch, R., Krischer, L., Megies, T., Behr, Y. & Wassermann, J., 2010. ObsPy: a Python toolbox for seismology, *Seismol. Res. Lett.,* **81**(3), 530–533.
Bird, P., 2003. An updated digital model of plate boundaries, *Geochem. Geophys. Geosyst.,* **4**(3), doi:10.1029/2001GC000252.
Brocher, T.M., 2005. Empirical relations between elastic wavespeeds and density in the Earth's crust, *Bull. seism. Soc. Am.,* **95**(6), 2081–2092.
Bürgmann, R. & Dresen, G., 2008. Rheology of the lower crust and upper mantle: evidence from rock mechanics, geodesy, and field observations, *Annu. Rev. Earth Planet. Sci.,* **36**(1), 531–567.
Castagna, J.P., Batzle, M.L. & Eastwood, R.L., 1985. Relationships between compressional-wave and shear-wave velocities in clastic silicate rocks. *Geophysics,* **50**(4), 571–581.
Crawford, W.C., Webb, S.C. & Hildebrand, J.A., 1998. Estimating shear velocities in the oceanic crust from compliance measurements by two-dimensional finite difference modeling fractured, *J. geophys. Res.,* **103**(B5), 9895–9916.
Dahm, T., Tillmann, F. & Morgan, J.P., 2006. Seismic broadband ocean-bottom data and noise observed with free-fall stations: experiences from long-term deployments in the North Atlantic and the Tyrrhenian Sea, *Bull. seism. Soc. Am.,* **96**(2), 647–664.
Du, Z.J. & Foulger, G.R., 1999. The crustal structure beneath the northwest fjords, Iceland, from receiver functions and surface waves, *Geophys. J. Int.,* **139**(2), 419–432.
Dziewonski, A.M. & Anderson, D.L., 1981. Preliminary reference Earth model, *Phys. Earth planet. Inter.,* **25**(4), 297–356.
Faul, U.H. & Jackson, I., 2005. The seismological signature of temperature and grain size variations in the upper mantle, *Earth planet. Sci. Lett.,* **234**(1–2), 119–134.
Fryer, P.B., 2002. Recent Studies of Serpentinite Occurrences in the Oceans: Mantle-Ocean Interactions in the Plate Tectonic Cycle, *Chemie der Erde - Geochemistry,* **62**(4), 257–302.
Gao, H. & Shen, Y., 2015. A Preliminary Full-Wave Ambient-Noise Tomography Model Spanning from the Juan de Fuca and Gorda Spreading Centers to the Cascadia Volcanic Arc, *Seismol. Res. Lett.,* **86**(5), 1253–1260.
Hannemann, K., Krüger, F. & Dahm, T., 2014. Measuring of clock drift rates and static time offsets of ocean bottom stations by means of ambient noise, *Geophys. J. Int.,* **196**(2), 1034–1042.
Haskell, N.A., 1962. Crustal reflection of plane P and SV waves, *J. geophys. Res.,* **67**(12), 4751–4768.
Horen, H., Zamora, M. & Dubuisson, G., 1996. Seismic waves velocities and anisotropy in serpentinized peridotites from xigaze ophiolite: abundance of serpentine in slow spreading ridge, *Geophys. Res. Lett.,* **23**(1), 9–12.
Julià, J., 2007. Constraining velocity and density contrasts across the crust - mantle boundary with receiver function amplitudes, *Geophys. J. Int.,* **171**(1), 286–301.
Julià, J., Ammon, C.J., Herrmann, R.B. & Correig, A.M., 2000. Joint inversion of receiver function and surface wave dispersion observations. *Geophys. J. Int.,* **143**(1), 99–112.
Jung, H., 2001. Water-induced fabric transitions in olivine, *Science,* **293**(5534), 1460–1463.
Kanamori, H., 1993. W Phase, *Geophys. Res. Lett.,* **20**(16), 1691–1694.
Karato, S.-I., 2012. On the origin of the asthenosphere, *Earth planet. Sci. Lett.,* **321–322,** 95–103.

Downloaded from http://gji.oxfordjournals.org/ at GEOMAR Helmholtz-Zentrum fuer Ozeanforschung Kiel on November 23, 2016

Kennett, B.L.N., Engdahl, E.R. & Buland, R., 1995. Constraints on seismic velocities in the Earth from traveltimes, *Geophys. J. Int.,* **122**(1), 108–124.

Kieling, K., Rössler, D. & Krüger, F., 2011. Receiver function study in northern Sumatra and the Malaysian peninsula, *J. Seismol.,* **15**(2), 235–259.

Kind, R., Kosarev, G.L. & Petersen, N.V., 1995. Receiver functions at the stations of the German Regional Seismic Network (GRSN), *Geophys. J. Int.,* **121**(1), 191–202.

Knott, C.G., 1899. Reflection and refraction of elastic waves with seismological application, *Phil. Mag. Ser. 5,* **48**(290), 64–97.

Krüger, F., 1994. Sediment structure at GRF from polarization analysis of *P* waves of nuclear explosions, *Bull. seism. Soc. Am.*, **84**(1), 149–170.

Kumar, P., 2015. Estimation of shear velocity contrast for dipping or anisotropic medium from transmitted Ps amplitude variation with ray-parameter, *Geophys. J. Int.,* **203**(3), 2248–2260.

Kumar, P., Sen, M.K. & Haldar, C., 2014. Estimation of shear velocity contrast from transmitted Ps amplitude variation with ray-parameter, *Geophys. J. Int.,* **198**(3), 1431–1437.

Laske, G., Masters, G., Ma, Z. & Pasyanos, M.E., 2013. CRUST1.0 : an updated global model of earth ' s Crust, *Geophys. Res. Abstracts,* Abstract EGU2013—-2658.

Maupin, V., 2011. Upper-mantle structure in southern Norway from beamforming of Rayleigh wave data presenting multipathing, *Geophys. J. Int.,* **185**(2), 985–1002.

McNamara, D.E. & Buland, R.P., 2004. Ambient noise levels in the continental United States, *Bull. seism. Soc. Am.*, **94**(4), 1517–1527.

Müller, G., 1985. The reflectivity method: a tutorial, *J. Geophys.,* **58,** 153–174.

Müller, R.D., Sdrolias, M., Gaina, C. & Roest, W.R., 2008. Age, spreading rates, and spreading asymmetry of the world's ocean crust, *Geochem. Geophys. Geosyst.,* **9**(4), doi:10.1029/2007GC001743.

Nguyen, X.N., Dahm, T. & Grevemeyer, I., 2009. Inversion of Scholte wave dispersion and waveform modeling for shallow structure of the Ninetyeast Ridge, *J. Seismol.*, **13**(4), 543–559.

Nuttli, O. & Whitmore, J.D., 1961. An observational determination of the variation of the angle of incidence of *P* waves with epicentral distance, *Bull. seism. Soc. Am.,* **51**(2), 269–276.

Nuttli, O. & Whitmore, J.D., 1962. On the determination of the polarization angle of the *S* wave, *Bull. seism. Soc. Am.*, **52**(1), 95–107.

Osen, A., Amundsen, L. & Reitan, A., 1999. Removal of water-layer multiples from multicomponent sea-bottom data, *Geophysics,* **64**(3), 838–851.

Ozacar, A.A. & Zandt, G., 2009. Crustal structure and seismic anisotropy near the San Andreas Fault at Parkfield, California, *Geophys. J. Int.,* **178**(2), 1098–1104.

Parolai, S., Bormann, P. & Milkereit, C., 2002. New relationships between Vs, thickness of sediments, and resonance frequency calculated by the H/V ratio of seismic noise for the cologne area (Germany), *Bull. seism. Soc. Am.,* **92**(6), 2521–2527.

Peterson, J., 1993. *Observations and Modeling of Seismic Background Noise*, U.S. Geological Survey Open-File Report, Albuquerque, New Mexico.

Phinney, R.A., 1964. Structure of the Earth's crust from spectral behavior of long-period body waves, *J. geophys. Res.,* **69**(14), 2997–3017.

Pilant, W.L., 1979. *Elastic Waves in the Earth,* Elsevier Scientific Publishing Company.

Ritzwoller, M.H. & Levshin, A.L., 2002. Estimating shallow shear velocities with marine multicomponent seismic data, *Geophysics,* **67**(6), 1991–2004.

Romanowicz, B., 2003. Global mantle tomography: progress status in the past 10 years, *Annu. Rev. Earth Planet. Sci.,* **31**(1), 303–328.

Rost, S. & Thomas, C., 2002. Array seismology: methods and applications. *Rev. Geophys.,* **40**(3), 1008, doi:10.1029/2000RG000100.

Scherbaum, F., 2001. *Of Poles and Zeros. Fundamentals of Digital Seismology,* 2nd edn, Springer.

Schiffer, C., Jacobsen, B.H., Balling, N., Ebbing, J. & Nielsen, S.B., 2015. The East Greenland Caledonides–teleseismic signature, gravity and isostasy, *Geophys. J. Int.,* **203**(2), 1400–1418.

Stachnik, J.C., Sheehan, A.F., Zietlow, D.W., Yang, Z., Collins, J. & Ferris, A., 2012. Determination of New Zealand ocean bottom seismometer orientation via Rayleigh-wave polarization, *Seismol. Res. Lett.,* **83**(4), 704–713.

Stähler, S.C. *et al.*, 2016. Preliminary performance report of the RHUM-RUM ocean bottom seismometer network around La Réunion, western Indian Ocean, *Adv. Geosci.,* **41,** 43–63.

Stammler, K., 1993. Seismichandler–programmable multichannel data handler for interactive and automatic processing of seismological analyses, *Comput. Geosci.,* **19**(2), 135–140.

Stixrude, L. & Lithgow-Bertelloni, C., 2005. Mineralogy and elasticity of the oceanic upper mantle: origin of the low-velocity zone, *J. geophys. Res.,* **110**(3), 1–16.

Sumy, D.F., Lodewyk, J.A., Woodward, R.L. & Evers, B., 2015. Ocean-bottom seismograph performance during the Cascadia Initiative, *Seismol. Res. Lett.,* **86**(5), 1238–1246.

Svenningsen, L. & Jacobsen, B.H., 2007. Absolute S-velocity estimation from receiver functions, *Geophys. J. Int.,* **170**(3), 1089–1094.

Thorwart, M. & Dahm, T., 2005. Wavefield decomposition for passive ocean bottom seismological data, *Geophys. J. Int.,* **163**(2), 611–621.

Wang, R., 1999a. A simple orthonormalization method for stable and efficient computation of Green's functions, *Bull. seism. Soc. Am.,* **89**(3), 733–741.

Wang, Y., 1999b. Approximations to the Zoeppritz equations and their use in AVO analysis, *Geophysics,* **64**(6), 1920–1927.

Webb, S.C., 1998. Broadband seismology and noise under the ocean, *Rev. Geophys.,* **36**(1), 105–142.

Weidle, C. & Maupin, V., 2008. An upper-mantle S-wave velocity model for Northern Europe from Love and Rayleigh group velocities, *Geophys. J. Int.,* **175**(3), 1154–1168.

Wessel, P., Smith, W.H.F., Scharroo, R., Luis, J. & Wobbe, F., 2013. Generic Mapping Tools: improved version released, *EOS, Trans. Am. geophys. Un.,* **94**(45), 409–410.

White, R.S., McKenzie, D. & O'Nions, R.K., 1992. Oceanic crustal thickness from seismic measurements and rare earth element inversions, *J. geophys. Res.,* **97**(B13), 19 683–19 715.

Wiechert, E., 1907. Über Erdbebenwellen. Part I: Theoretisches über die Ausbreitung der Erdbebenwellen, *Nachrichten von der Gesellschaft der Wissenschaften zu Göttingen, Mathematisch-Physikalische Klasse,* 415–529.

Yamamoto, T. & Torii, T., 1986. Seabed shear modulus profile inversion using surface gravity (water) wave-induced bottom motion, *Geophys. J. R. astr. Soc.*, **85**(2), 413–431.

Zhu, L. & Kanamori, H., 2000. Moho depth variation in southern California from teleseismic receiver functions, *J. geophys. Res.,* **105**(B2), 2969–2980.

Zitellini, N. *et al.*, 2009. The quest for the Africa-Eurasia plate boundary west of the Strait of Gibraltar, *Earth planet. Sci. Lett.,* **280**(1–4), 13–50.

Zoeppritz, K., 1919. Über Erdbebenwellen Part VII b . Über Reflexion und Durchgang seismischer Wellen durch Unstetigkeitsflaechen, *Nachrichten von der Gesellschaft der Wissenschaften zu Göttingen, Mathematisch-Physikalische Klasse,* 66–84.

SUPPORTING INFORMATION

Additional Supporting Information may be found in the online version of this paper:

Figure S1. Global velocity model used for synthetic seismograms (teleseismic case). The model is split into a source and a receiver model. The source model is continental PREM (dashed lines, Dziewonski & Anderson 1981). Here, we present a possible receiver model above 155.05 km depth with the CRUST 1.0 model for the location 38.5°N and −18.5°E (solid lines, Laske *et al*. 2013).

Figure S2. Test for influence of 5 per cent noise on the appearance of $v_{s,\mathrm{app}}$ profiles for the synthetic model CM-REF. The spectral

Downloaded from http://gji.oxfordjournals.org/ at GEOMAR Helmholtz-Zentrum fuer Ozeanforschung Kiel on November 23, 2016

appearance of the noise was fitted to the actual noise spectrum using the sum of a low pass filtered (0.02 Hz, order 1) and band pass filtered (0.2–0.5 Hz, order 2) random noise. The grey dots show the results of 300 trails. The blue curve shows the $v_{s,\mathrm{app}}$ profile for the undisturbed CM-REF data. The yellow curve shows the mean and the orange the median of all estimates.

Figure S3. Test for influence of Wiener filter parameter (deconvolution time window length and damping parameter) on the appearance of $v_{s,\mathrm{app}}$ profiles. The colours indicate the damping parameter. (a)–(e) Grid search results for deconvolution time window length between 30 and 230 s.
(http://gji.oxfordjournals.org/lookup/suppl/doi:10.1093/gji/ggw342/-/DC1)

Please note: Oxford University Press is not responsible for the content or functionality of any supporting materials supplied by the authors. Any queries (other than missing material) should be directed to the corresponding author for the paper.

Downloaded from http://gji.oxfordjournals.org/ at GEOMAR Helmholtz-Zentrum fuer Ozeanforschung Kiel on November 23, 2016